SIAM J. Imaging Sciences
Vol. 13, No. 4, pp. 2250–2280

Imaging with the Elliptic Radon Transform in Three Dimensions from an Analytical and Numerical Perspective*

Christine Grathwohl†, Peer Christian Kunstmann†, Eric Todd Quinto‡, and Andreas Rieder†

Abstract. The three-dimensional elliptic Radon transform (eRT) averages distributions over ellipsoids of revolution. It thus serves as a linear model in seismic imaging where one wants to recover the earth's interior from reflected wave fields. As there is no inversion formula known for the eRT, approximate formulas have to be used. In this paper we suggest several of those, microlocally analyze their properties, and provide and implement an adapted algorithm whose performance we test by diverse numerical experiments. Our previous results of [*Inverse Problems*, 34 (2018), 014002, 114001] are thus generalized to three space dimensions.

Key words. generalized Radon transforms, Fourier integral operators, microlocal analysis, seismic imaging

AMS subject classifications. 58J40, 57R45, 86A15, 86A22, 35S30

DOI. 10.1137/20M1332657

1. Introduction.

The elliptic Radon transform F serves as a model in seismic imaging when sources and receivers are offset by a constant vector and linearization has been performed about a constant background sound speed. One is led to solve the linear equation $Fn = y$ where y represents preprocessed measurements of the reflected acoustic wave fields and n represents the high frequency content of the searched-for true speed of sound. As there is no inversion formula known in this geometric setting, one has to find, study, and implement more general approximate inversion schemes.

For instance, in Kirchhoff migration, the classical inversion scheme of geophysics, one applies a kind of convolution operator K followed by a dual transform (generalized backprojection) $F^\sharp$ to the data to obtain $F^\sharp Ky$. Instead of n we thus recover $F^\sharp KFn$. The *imaging operator* $F^\sharp KF$ is the sum of a low pass filter (partial identity) and a smoothing operator; see [3]. Consequently, some of the features of n are indeed visible in $F^\sharp KFn$.

Another approach consists of applying F^*, the formal L^2-adjoint (backprojection), yielding the normal operator $F^*\psi F$ as imaging operator (ψ is a smooth cutoff function needed for technical reasons; see start of section 3 below). Imaging properties of $F^*\psi F$ in different settings have been analyzed by many authors including [7, 8, 19, 23, 25].

*Received by the editors April 20, 2020; accepted for publication (in revised form) October 2, 2020; published electronically December 15, 2020.

https://doi.org/10.1137/20M1332657

Funding: The work of the authors was supported by the Deutsche Forschungsgemeinschaft (DFG, German Research Foundation) project ID 258734477, SFB 1173. The work of the third author was partially supported by National Science Foundation grant DMS-1712207 and the Tufts University Faculty Research Awards Committee. The authors received no financial benefit from this work.

†Department of Mathematics, Karlsruhe Institute of Technology (KIT), D-76128 Karlsruhe, Germany (chrgra@web.de, peer.kunstmann@kit.edu, andreas.rieder@kit.edu).

‡Department of Mathematics, Tufts University, Medford, MA 02155 USA (todd.quinto@tufts.edu).

In our two previous papers [11, 12] (see also [22]) we have contributed to this research twofold. First, we have augmented the normal operator by a properly supported pseudodifferential operator K of positive order so that $KF^*\psi F$ enhances features (discontinuities) of n. In contrast, the abovementioned two examples deliver rather smooth versions of n. Further, we have microlocally analyzed these operators in two spatial dimensions to understand how they map singularities. Using this knowledge, we have been able to construct K with useful imaging properties. Second, also in two spatial dimensions, we have developed and implemented a corresponding regularization scheme based on the approximate inverse [16]. The present paper extends our two-dimensional results to three space dimensions. By no means is this generalization trivial: the microlocal analysis is more involved and the implementation of the numerical scheme poses additional challenges.

Our material is organized as follows. In the next section we briefly recall how the seismic model with the elliptic Radon transform is obtained by linearizing the acoustic wave equation. Then, we introduce our first imaging operator in section 3 and analyze it microlocally, which leads us to define new operators with improved imaging properties. To give a somewhat self-contained presentation, we provide basic concepts from microlocal analysis. Section 4 is devoted to our numerical scheme where implementation issues are discussed in some detail. Finally, we report and comment on numerical experiments not only to illustrate our microlocal predictions (section 5.1) but also to test the robustness of the numerical scheme with respect to noise in the offset and modeling error (section 5.2). Moreover, we discuss the formation of artifacts appearing in the reconstructions. A sound microlocal explanation remains to be given, though, in future research.

2. The forward operator. A well-established method to investigate the subsurface of the earth is to generate pressure waves on the surface and measure their returning reflections. For simplification we assume that no shear waves occur and that the earth has constant mass density. Then, wave propagation with sound speed ν is described by the acoustic wave equation

$$\frac{1}{\nu^2(x)}\partial_t^2 u(t,x;\mathbf{x}_\mathrm{s}) - \Delta u(t,x;\mathbf{x}_\mathrm{s}) = \delta(x-\mathbf{x}_\mathrm{s})\delta(t) \tag{2.1}$$

for time $t \geq 0$ at location $x \in \mathbb{R}^3$ with source location $\mathbf{x}_\mathrm{s}$. We augment (2.1) with vanishing initial conditions

$$u(0,\,\cdot\,;\mathbf{x}_\mathrm{s}) = \partial_t u(0,\,\cdot\,;\mathbf{x}_\mathrm{s}) = 0 \tag{2.2}$$

(interpreted in a distributional sense) since the environment is at rest before the wave is excited. The task is to reconstruct the speed of sound ν from the backscattered field $u(t,\mathbf{x}_\mathrm{r};\mathbf{x}_\mathrm{s})$ observed at a receiver point $\mathbf{x}_\mathrm{r}$ for $(t,\mathbf{x}_\mathrm{r};\mathbf{x}_\mathrm{s}) \in [0,T_\mathrm{max}] \times \mathcal{R} \times \mathcal{S}$, where T_max is the recording time and $\mathcal{R}$ and $\mathcal{S}$ are the sets of receiver and source positions, respectively.

We consider the common offset scanning geometry where the distance of source to receiver is a constant vector. This geometry is realized by

$$\mathbf{x}_\mathrm{s} = \mathbf{x}_\mathrm{s}(s) = (s_1, s_2-\alpha, 0)^\top \quad \text{and} \quad \mathbf{x}_\mathrm{r} = \mathbf{x}_\mathrm{r}(s) = (s_1, s_2+\alpha, 0)^\top$$

for a fixed offset $\alpha \geq 0$ and $(s_1, s_2) \in S_0 \subseteq \mathbb{R}^2$, where S_0 is a nonempty open, bounded, and connected subset of $\mathbb{R}^2$.

To solve the inverse problem, we make the classical ansatz

$$\frac{1}{\nu^2(x)} = \frac{1+n(x)}{c^2}$$

for $x \in \mathbb{R}^3$ with a constant and a priori known background velocity c, say, $c = 1$, and a function n being compactly supported in $\mathbb{R}^3_+ := \{x \in \mathbb{R}^3 \,|\, x_3 > 0\}$ (the x_3-axis points downward). In doing so we are seeking n instead of ν. Physically the quantity n can be interpreted as a kind of reflectivity, which captures the high frequency variations of ν; see [4, sect. 3.2.1].

The solution $\widetilde{u}$ of (2.1) and (2.2) for $\nu = c = 1$ is our reference solution:

$$\partial_t^2 \widetilde{u}(t, x; \mathbf{x}_\mathrm{s}(s)) - \Delta \widetilde{u}(t, x; \mathbf{x}_\mathrm{s}(s)) = \delta(x - \mathbf{x}_\mathrm{s}(s))\delta(t). \tag{2.3}$$

We follow the lines of [6] and [26] to derive a linear equation for n. For further details see [10] and [12].

By the Born approximation we derive the following representation of $u - \widetilde{u}$:

$$\begin{aligned}(u - \widetilde{u})(t, \mathbf{x}_\mathrm{r}(s); \mathbf{x}_\mathrm{s}(s)) \\ = -\partial_t^2 \int_{\mathbb{R}^3_+} a_{\mathbf{x}_\mathrm{s}(s)}(x) a_{\mathbf{x}_\mathrm{r}(s)}(x) n(x) \delta(t - \tau_{\mathbf{x}_\mathrm{s}(s)}(x) - \tau_{\mathbf{x}_\mathrm{r}(s)}(x))\, \mathrm{d}x\end{aligned} \tag{2.4}$$

with

$$a_y(x) = \frac{1}{4\pi|x-y|} \qquad \text{and} \qquad \tau_y(x) = |x - y|.$$

Using the abbreviations

$$A(s, x) := 16\pi^2 a_{\mathbf{x}_\mathrm{s}(s)}(x) a_{\mathbf{x}_\mathrm{r}(s)}(x) = \frac{1}{|\mathbf{x}_\mathrm{s}(s) - x||x - \mathbf{x}_\mathrm{r}(s)|}$$

and

$$\varphi(s, x) := \tau_{\mathbf{x}_\mathrm{s}(s)}(x) + \tau_{\mathbf{x}_\mathrm{r}(s)}(x) = |\mathbf{x}_\mathrm{s}(s) - x| + |x - \mathbf{x}_\mathrm{r}(s)|,$$

we define the operator

$$Fn(s, t) := \int_{\mathbb{R}^3_+} n(x) A(s, x) \delta(t - \varphi(s, x))\, \mathrm{d}x, \quad (s, t) \in S_0 \times (2\alpha, \infty).$$

Next, we integrate (2.4) two times with respect to t to get

$$Fn(s, t) = y(s, t)$$

with right-hand side

$$y(s, t) = -16\pi^2 \int_0^t (t - r)(u - \widetilde{u})(r, \mathbf{x}_\mathrm{r}(s); \mathbf{x}_\mathrm{s}(s))\, \mathrm{d}r, \tag{2.5}$$

which is known from the measurements and from the reference solution (2.3).

Note that F is a generalized Radon transform which integrates over open half ellipsoids

$$E(s,t) = \left\{x \in \mathbb{R}^3_+ \,|\, \varphi(s,x) = t\right\} = \left\{x \in \mathbb{R}^3_+ \,|\, |\mathbf{x}_\mathrm{s}(s) - x| + |x - \mathbf{x}_\mathrm{r}(s)| = t\right\}.$$

We refer to [21, Def. 2.1] for the definition of generalized Radon transforms. More details are given in [10, sect. 3.1]. Moreover, F is a Fourier integral operator (see [14] for the definition), which can be written as

$$\begin{aligned} Ff(s,t) &= \int_{\mathbb{R}^3_+} f(x)\delta(t-\varphi(s,x))A(s,x)\,\mathrm{d}x \\ &= \frac{1}{2\pi}\int_{\mathbb{R}}\int_{\mathbb{R}^3_+} f(x)A(s,x)\mathrm{e}^{\mathrm{i}\omega(t-\varphi(s,x))}\,\mathrm{d}x\,\mathrm{d}\omega \end{aligned} \tag{2.6}$$

for $f \in C_c^\infty(\mathbb{R}^3_+)$. The functions $(s,t,x,\omega) \mapsto \frac{1}{2\pi}A(s,x)$ for $(s,t,x,\omega) \in S_0 \times (2\alpha,\infty) \times \mathbb{R}^3_+ \times \mathbb{R}$ and $(s,t,x,\omega) \mapsto \omega(t-\varphi(s,x))$ are the symbol and the phase of F, respectively.

3. Imaging.

To the best of our knowledge there is no formula known to reconstruct n directly from the elliptic means $g = Fn$ in case $\alpha > 0$. Therefore, we define the imaging operator

$$\Lambda := -\Delta\partial_3 F^*\psi F, \tag{3.1}$$

which was introduced in [22] for $\alpha = 0$ based on an inversion formula of [1]. So, instead of n we are able to reconstruct at least Λn from g. Here, Δ is the Laplace operator, ∂_3 the derivative in third space direction (downward), and ψ is a function in $C_c^\infty(S_0 \times (2\alpha,\infty))$. Further, F^* is dual to F and given by

$$\begin{aligned} F^*g(x) &= \int_{S_0\times(2\alpha,\infty)} g(s,t)\delta(t-\varphi(s,x))A(s,x)\,\mathrm{d}(s,t) \\ &= \frac{1}{2\pi}\int_{\mathbb{R}}\int_{S_0\times(2\alpha,\infty)} g(s,t)A(s,x)\mathrm{e}^{\mathrm{i}\omega(t-\varphi(s,x))}\,\mathrm{d}(s,t)\,\mathrm{d}\omega \end{aligned} \tag{3.2}$$

for $g \in C_c^\infty(S_0 \times (2\alpha,\infty))$ and $x \in \mathbb{R}^3_+$. The cutoff function ψ is needed to have a well-defined composition of F^* with F as $F\colon \mathcal{E}'(\mathbb{R}^3_+) \to \mathcal{D}'(S_0 \times (2\alpha,\infty))$ and $F^*\colon \mathcal{E}'(S_0 \times (2\alpha,\infty)) \to \mathcal{D}'(\mathbb{R}^3_+)$. Our Λ is a special case of imaging operators investigated in [12]. Moreover, it is a pseudodifferential operator of order 1 [12, Thm. 3.3], which makes it useful for imaging purposes as we explain in the following section.

3.1. Pseudodifferential operators and microlocal analysis.

Our theoretical results are based on the theory of pseudodifferential operators and their microlocal properties. The following basic concepts can be found in many textbooks; we refer, e.g., to [20].

Definition 3.1 (pseudodifferential symbol). *Let $d \in \mathbb{N}$ and $X \subseteq \mathbb{R}^d$ be open. A* symbol of order $m \in \mathbb{R}$ *is a function $p = p(x,\xi) \in C^\infty(X \times \mathbb{R}^d)$ satisfying, for every compact set $\mathrm{K} \subseteq X$ and for each pair of multi-indices α, β there exists a constant $C = C(\mathrm{K},\alpha,\beta)$ such that, for all $x \in \mathrm{K}$ and all $\xi \in \mathbb{R}^d$,*

$$\left|D_\xi^\alpha D_x^\beta p(x,\xi)\right| \le C(1+|\xi|)^{m-|\alpha|}.$$

The set of symbols of order m on X is denoted by $S^m(X)$.

A symbol $p \in S^m(X)$ is microlocally elliptic of order m *at $(x_0,\xi_0) \in X \times \mathbb{R}^d\backslash\{0\}$ if there are an open neighborhood U of x_0 in X, a conic neighborhood V of ξ_0 in $\mathbb{R}^d\backslash\{0\}$, and constants $M > 0$ and $C > 0$ such that*

$$|p(x,\xi)| \ge C(1+|\xi|)^m$$

for all $x \in U$ and all $\xi \in V$ with $|\xi| \ge M$.

Note that $S^m(X)$ is the standard symbol class of Hörmander [14, Def. 1.1.1].

Definition 3.2 (pseudodifferential operator). *Let $X \subseteq \mathbb{R}^d$ be open and $m \in \mathbb{R}$. Then, the linear operator $P\colon \mathcal{D}(X) \to \mathcal{E}(X)$ is a* pseudodifferential operator of order m *if there is a pseudodifferential symbol p of order m such that for all $f \in \mathcal{D}(X)$,*

$$Pf(y) = \int_{\mathbb{R}^d}\int_X \mathrm{e}^{\mathrm{i}(y-x)\cdot\xi} p(x,\xi) f(x)\,\mathrm{d}x\,\mathrm{d}\xi.$$

The function p is called the full symbol *of the operator P. The* principal symbol $\sigma(P)$ of P *is the equivalence class of p in the quotient space $S^m(X)/S^{m-1}(X)$.*

The operator P is microlocally elliptic *if its symbol is microlocally elliptic.*

Please note that the integral defining P in the above definition exists as an *oscillatory integral* and represents a distribution in general [14, Chap. I]. Further, any pseudodifferential operator can be extended as an operator mapping $\mathcal{E}'(X)$ continuously into $\mathcal{D}'(X)$. We tacitly rely on this extension throughout the paper.

Definition 3.3. *A function $f\colon \mathbb{R}^d \to \mathbb{C}$ is* rapidly decaying at infinity *on the cone $V \subseteq \mathbb{R}^d$ if for every $N \in \mathbb{N}$ there is a constant $C = C(N) > 0$ such that*

$$|f(\xi)| \le C(1+|\xi|)^{-N}$$

for all $\xi \in V$.

Definition 3.4. *Let $\Omega \subseteq \mathbb{R}^d$ be open. A distribution $u \in \mathcal{D}'(\Omega)$ is* microlocally C^∞ *at $(x_0,\xi_0) \in \Omega \times \mathbb{R}^d\backslash\{0\}$ if for some $\phi \in C_c^\infty(\Omega)$ with $\phi(x_0) \ne 0$ and some conic neighborhood V of ξ_0 in $\mathbb{R}^d\backslash\{0\}$, the Fourier transform $\widehat{\phi u}$ is rapidly decaying on V.*

As an image carries most of its information content at singularities, we are interested in characterizing their location and direction. Those are collected in the *wave front set* of a distribution u:

$$\mathrm{WF}(u) = \{(x,\xi) \in \Omega \times \mathbb{R}^d \setminus \{0\} \,|\, u \text{ is not microlocally } C^\infty \text{ at } (x,\xi)\}. \tag{3.3}$$

Theorem 3.5 (pseudolocal property). *Let $u \in \mathcal{E}'(\Omega)$. If P is a pseudodifferential operator, it holds that*

$$\mathrm{WF}(Pu) \subseteq \mathrm{WF}(u).$$

If P is microlocally elliptic at $(x_0, \xi_0) \in \Omega \times \mathbb{R}^d$, then

$$(x_0, \xi_0) \in \mathrm{WF}(u) \text{ if and only if } (x_0, \xi_0) \in \mathrm{WF}(Pu).$$

If P is microlocally elliptic at every $(x, \xi) \in \Omega \times \mathbb{R}^d$, then we even have

$$\mathrm{WF}(Pu) = \mathrm{WF}(u).$$

Next, we refine the concept of wave front sets of a distribution by a microlocalization of H^s in lieu of C^∞. A distribution $u \in \mathcal{D}'(\Omega)$ is *microlocally H^r* at $(x_0, \xi_0) \in \Omega \times \mathbb{R}^d \backslash \{0\}$ if for some neighborhood U of x_0 in Ω and some conic neighborhood V of ξ_0 in $\mathbb{R}^d \backslash \{0\}$ we have

$$\int_V |\widehat{\phi u}(\xi)|^2 (1 + |\xi|^2)^r \, \mathrm{d}\xi < \infty$$

for all $\phi \in C_c^\infty(U)$. Now, for $r \in \mathbb{R}$, the *H^r-wave front set of u* is

$$\mathrm{WF}^r(u) = \{(x, \xi) \in \Omega \times \mathbb{R}^d \setminus \{0\} \,|\, u \text{ is not microlocally } H^r \text{ at } (x, \xi)\}.$$

Wave front sets and H^r-wave front sets are connected via $\mathrm{WF}(u) = \mathrm{cl}\big(\cup_{r \in \mathbb{R}} \mathrm{WF}^r(u) \big)$.

Theorem 3.6. *Let P be a pseudodifferential operator of order m. If P is microlocally elliptic at (x_0, ξ_0), we have*

$$(x_0, \xi_0) \in \mathrm{WF}^r(u) \text{ if and only if } (x_0, \xi_0) \in \mathrm{WF}^{r-m}(Pu)$$

for $u \in \mathcal{E}'(\Omega)$ and $r \in \mathbb{R}$.

We now provide a classification of operators' effects on singularities.

Definition 3.7. *Let Ω be an open subset of $\mathbb{R}^d$ and let $P \colon \mathcal{E}'(\Omega) \to \mathcal{D}'(\Omega)$ be continuous and linear.*

Let $u \in \mathcal{E}'(\Omega)$ and $(x, \xi) \in \mathrm{WF}(u)$. Then, (x, ξ) is a visible singularity of u with respect to P *(visible singularity) if $(x, \xi) \in \mathrm{WF}(Pu)$. On the other hand, (x, ξ) is an* invisible singularity of u with respect to P *(invisible singularity) if $(x, \xi) \notin \mathrm{WF}(Pu)$.*

If $(y, \eta) \in \mathbb{R}^d \times \mathbb{R}^d \setminus \{0\}$, then (y, η) is a (nonsmooth) artifact *in Pu if $(y, \eta) \in \mathrm{WF}(Pu)$ but $(y, \eta) \notin \mathrm{WF}(u)$.*

Let P be a pseudodifferential operator. By Theorem 3.5, P generates no artifacts and, if P is microlocally elliptic at any pair in $\Omega \times \mathbb{R}^d$, then all singularities are visible.

This description of singularities and artifacts is well-defined theoretically but there can be issues applying it in practice. For example, visible singularities might be in $\mathrm{WF}(Pu)$ but the values of the reconstruction at the singularity could be so close to those in the surrounding area that they are effectively not visible in the reconstruction Pu.

In practice, regularization can smooth reconstructions, so nonsmooth artifacts can be smoothed; that is, they are C^∞. Nevertheless, they can still appear as visual artifacts (e.g., additional streaks) in the reconstruction.

3.2. The symbols of $F^*\psi F$ and Λ. To determine the top order symbol of Λ, we investigate the normal operator

$$(F^*\psi Fn)(x) = \frac{1}{2\pi}\int_{\mathbb{R}^3_+}\int_{\mathbb{R}}\int_{\mathbb{R}^2}\psi(s,\varphi(s,x))A(s,x)A(s,y)n(y)\mathrm{e}^{\mathrm{i}\omega(\varphi(s,x)-\varphi(s,y))}\,\mathrm{d}s\,\mathrm{d}\omega\,\mathrm{d}y \tag{3.4}$$

for $n \in C_c^\infty(\mathbb{R}^3_+)$ and $x \in \mathbb{R}^3_+$.

Theorem 3.8. *The wave front set* $\mathrm{WF}(F^*\psi Fu)$ *satisfies*

$$\mathrm{WF}(F^*\psi Fu) \subseteq \{(x,\xi;x,\xi) \in (\mathbb{R}^3_+ \times \mathbb{R}^3 \setminus \{0\}) \times (\mathbb{R}^3_+ \times \mathbb{R}^3 \setminus \{0\}) \mid \text{there exists } s \in S_0 \text{ and } \omega \neq 0 \text{ such that } \xi = \omega\nabla_x\varphi(s,x)\} \circ \mathrm{WF}(u)$$

for $u \in \mathcal{E}'(\mathbb{R}^3_+)$. *Here, the operation* $\circ$ *denotes the usual composition of general relations.*

One proves Theorem 3.8 analogously to Theorem 4 of [15]. A detailed proof can be found in [10, Thm. 3.15].

In [12, Thm. 3.5] we proved explicit representations of the top order symbol for a class of operators that includes Λ, and thus Theorem 3.9 below is a special case. However, the proof is rather technical and requires deep knowledge of measure theory and differential geometry. Here, we lay out a different path, which is confined to the theory of pseudodifferential operators. We adapt and extend ideas of [2].

For technical reasons we need to modify $F^*\psi F$ as well as Λ: for $\delta > 0$ define $\zeta_\delta \in C^\infty(\mathbb{R}^3_+,\mathbb{R})$ by

$$\zeta_\delta(y) = 1 \quad \text{if } y_3 \geq 2\delta \qquad \text{and} \qquad \zeta_\delta(y) = 0 \quad \text{if } y_3 < \delta.$$

Then, we set

$$F^*\psi F_\delta := F^*\psi F\zeta_\delta \quad \text{and} \quad \Lambda_\delta := \Lambda\zeta_\delta = -\Delta\partial_3 F^*\psi F_\delta.$$

In view of (3.4) we have

$$(F^*\psi F_\delta n)(x) = \frac{1}{2\pi}\int_{\mathbb{R}^3_+}\int_{\mathbb{R}}\int_{\mathbb{R}^2}\psi(s,\varphi(s,x))A(s,x)A(s,y)\zeta_\delta(y)n(y)\mathrm{e}^{\mathrm{i}\omega(\varphi(s,x)-\varphi(s,y))}\,\mathrm{d}s\,\mathrm{d}\omega\,\mathrm{d}y. \tag{3.5}$$

Since n is compactly supported in $\mathbb{R}^3_+$, we have $\Lambda_\delta n = \Lambda n$ for δ sufficiently small. Of course, the size of δ depends on n.

We are now ready to present the top order symbol Λ_δ.

Theorem 3.9. *The operator* Λ_δ *is a sum of a pseudodifferential operator and a smoothing operator.*[1]

[1] A smoothing operator maps all compactly supported distributions to C^∞ functions. For the study of singularities, those operators can be neglected.

Let $(x,\xi) \in \mathbb{R}^3_+ \times \mathbb{R}^3$ *with* $\xi_3 \neq 0$. *If there exist* $s \in S_0$ *and* $\omega \in \mathbb{R}\backslash\{0\}$ *such that* $\xi = \omega \nabla_x \varphi(s,x)$, *then*

$$\sigma(\Lambda_\delta)(x,\xi) = (2\pi)^5 \mathrm{i}\xi_3 |\xi|^2 \frac{\psi(s(x,\xi),\varphi(s(x,\xi),x))A(s(x,\xi),x)^2 \zeta_\delta(x)}{|\omega(x,\xi)|^2 |B(s(x,\xi),x)|}. \tag{3.6}$$

Here,

$$B(s(x,\xi),x) = \det \begin{pmatrix} [\nabla_x \varphi](s(x,\xi),x)^\top \\ [\partial_{s_1} \nabla_x \varphi](s(x,\xi),x)^\top \\ [\partial_{s_2} \nabla_x \varphi](s(x,\xi),x)^\top \end{pmatrix}, \tag{3.7}$$

$$\omega(x,\xi) = \frac{\xi_3 |\mathbf{x}_\mathrm{s}(s(x,\xi)) - x||x - \mathbf{x}_\mathrm{r}(s(x,\xi))|}{x_3(|\mathbf{x}_\mathrm{s}(s(x,\xi)) - x| + |x - \mathbf{x}_\mathrm{r}(s(x,\xi))|)}, \tag{3.8}$$

and

$$s_1(x,\xi) = x_1 - \frac{\xi_1}{\xi_3} x_3,$$

$$s_2(x,\xi) = \begin{cases} x_2 - \frac{1}{2}\frac{\xi_3}{\xi_2}\left(\left(\frac{\xi_2^2-\xi_1^2}{\xi_3^2} - 1\right)x_3 + \sqrt{x_3^2\left(\frac{\xi_1^2+\xi_2^2}{\xi_3^2}+1\right)^2 + 4\alpha^2\frac{\xi_2^2}{\xi_3^2}}\right) & \text{for } \xi_2 \neq 0, \\ x_2 & \text{for } \xi_2 = 0. \end{cases}$$

If there is no $s \in S_0$ *satisfying* $\xi = \omega \nabla_x \varphi(s,x)$ *for some* $\omega \in \mathbb{R}\backslash\{0\}$, *we have* $\sigma(\Lambda_\delta) = 0$. *Moreover, for* $(x,\xi) \in \mathbb{R}^3_+ \times \mathbb{R}^3 \setminus \{0\}$ *with* $\xi_3 = 0$ *the top order symbol* $\sigma(\Lambda_\delta)$ *vanishes as well.*

Proof. We only sketch the main steps and refer to [10, Thm. 3.21] for the full proof.

First, we apply the transformation $\widetilde{s} = s\omega$ to the integral in (3.5). So, we obtain a representation of $F^*\psi F_\delta$ as a Fourier integral operator depending on x, y, and the phase variable $(\widetilde{s},\omega)$. Next, we employ the fact that an operator is smoothing if it vanishes in a conic neighborhood of a certain set (see [24, Prop. 2.1b]). In case of $F^*\psi F_\delta$ this set is characterized by the diagonal $x = y$. Therefore, for an $\varepsilon > 0$ we introduce the cutoff function $\widehat{\zeta}_\varepsilon \in C^\infty(\mathbb{R}^3_+ \times \mathbb{R}^3_+, \mathbb{R})$ with $0 \leq \widehat{\zeta}_\varepsilon \leq 1$,

$$\widehat{\zeta}_\varepsilon(x,y) = 1 \quad \text{if } |x-y| < \varepsilon \qquad \text{and} \qquad \widehat{\zeta}_\varepsilon(x,y) = 0 \quad \text{if } |x-y| > 2\varepsilon.$$

Using this function, we split $F^*\psi F_\delta$ into a sum of a smoothing operator and an operator which, by [24, Thm. 19.2], turns out to be a pseudodifferential operator if ε is sufficiently small. Then, we perform the transformation $\xi = \omega \nabla_x \varphi(\widetilde{s},\omega,x)$, expand the phase function in a Taylor polynomial about x, and introduce several different smooth cutoff functions to show the required assumptions. Finally, we apply expansion (2.1.4) of [14]. ∎

3.3. Microlocal properties. To understand how our imaging operator Λ maps, emphasizes, or deemphasizes singularities, we now analyze its top order symbol.

We introduce the ratios

$$p := p(\xi) = \frac{\xi_1}{\xi_3} \quad \text{and} \quad q := q(\xi) = \frac{\xi_2}{\xi_3}$$

for $\xi \in \mathbb{R}^3$ with $\xi_3 \neq 0$ and rewrite $\sigma(\Lambda_\delta)$ in terms of x, ξ_3, p, and q. We find that

$$\left\{(p,q) \in \mathbb{R}^2 \,|\, \exists \xi \in \mathbb{R}^3,\ \xi_3 \neq 0,\ p = \frac{\xi_1}{\xi_3},\ q = \frac{\xi_2}{\xi_3}\right\} = \mathbb{R}^2.$$

Hence, we consider $(p,q) \in \mathbb{R}^2$ in the following. By Theorem 3.9 we get $s(p,q,x) = (s_1(p,q,x), s_2(p,q,x))$ with

$$s_1(p,q,x) = x_1 - px_3 \quad \text{and} \quad s_2(p,q,x) = x_2 - x_3 Q\left(p,q,\frac{\alpha}{x_3}\right)$$

for $(p,q) \in \mathbb{R}^2$ and $x \in \mathbb{R}^3_+$ where

$$Q(p,q,\lambda) := \begin{cases} \frac{1}{2q}\left(q^2 - p^2 - 1 + \sqrt{(p^2+q^2+1)^2 + 4\lambda^2 q^2}\right) & \text{for } q \neq 0, \\ 0 & \text{for } q = 0, \end{cases}$$

for $(p,q) \in \mathbb{R}^2$ and $\lambda > 0$. Note that s_2 is smooth on its domain of definition [10, Rem. 3.13]. Further,

$$D_+ := D_+(p,q,x) := |x - \mathbf{x}_\mathrm{s}(s(p,q,x))| = x_3\sqrt{\left(Q\left(p,q,\frac{\alpha}{x_3}\right) + \frac{\alpha}{x_3}\right)^2 + p^2 + 1}$$

and analogously

$$D_- := D_-(p,q,x) = x_3\sqrt{\left(Q\left(p,q,\frac{\alpha}{x_3}\right) - \frac{\alpha}{x_3}\right)^2 + p^2 + 1}.$$

With these abbreviations we have

$$A(p,q,x) := A(s(p,q,x),x) = \frac{1}{D_+(p,q,x)}\frac{1}{D_-(p,q,x)}$$

and

$$\psi(p,q,x) := \psi(s(p,q,x), \varphi(s(p,q,x),x)) = D_+(p,q,x) + D_-(p,q,x).$$

By (3.8),

$$\omega(p,q,x,\xi_3) = \frac{\xi_3}{x_3}\frac{D_+(p,q,x) + D_-(p,q,x)}{D_+(p,q,x)D_-(p,q,x)}.$$

From (3.7) we obtain

$$B(s,x) = x_3\left(\frac{1}{|\mathbf{x}_\mathrm{s}(s) - x|} + \frac{1}{|x - \mathbf{x}_\mathrm{r}(s)|}\right)\left(\frac{1}{|\mathbf{x}_\mathrm{s}(s) - x|^2} + \frac{1}{|x - \mathbf{x}_\mathrm{r}(s)|^2}\right)$$
$$\left(1 + \frac{x - \mathbf{x}_\mathrm{s}(s)}{|\mathbf{x}_\mathrm{s}(s) - x|} \cdot \frac{x - \mathbf{x}_\mathrm{r}(s)}{|x - \mathbf{x}_\mathrm{r}(s)|}\right)$$

yielding

$$B(p,q,x) = x_3\left(\frac{1}{D_+(p,q,x)} + \frac{1}{D_-(p,q,x)}\right)\left(\frac{1}{D_+^2(p,q,x)} + \frac{1}{D_-^2(p,q,x)}\right)$$
$$\left(1 + \frac{\left(px_3, x_3 Q\left(p,q,\frac{\alpha}{x_3}\right) + \alpha, x_3\right)^\top}{D_+(p,q,x)} \cdot \frac{\left(px_3, x_3 Q\left(p,q,\frac{\alpha}{x_3}\right) - \alpha, x_3\right)^\top}{D_-(p,q,x)}\right).$$

In our numerical examples of section 5 below we will only consider functions n with supports a fixed distance away from the surface. This condition is also satisfied in geophysical applications. As a consequence, we need not and we do not distinguish any longer between the operators Λ and Λ_δ.

Proposition 3.10. *Let $(y,\eta) \in \mathbb{R}^3_+ \times \mathbb{R}^3\backslash\{0\}$ and define*

$$C(y) := \left\{\xi \in \mathbb{R}^3 \,|\, \xi_3 \neq 0, \psi(s(y,\xi), \varphi(s(y,\xi), y)) > 0\right\}.$$

If $\eta \in C(y)$, then Λ is microlocally elliptic of order 1 at (y,η).

Further, Λ is smoothing at $(x,\xi) \in \mathbb{R}^3_+ \times \mathbb{R}^3 \setminus \{0\}$ with $\xi \notin \overline{C(x)}$.

Proposition 3.10 can be used to determine visible and invisible singularities with respect to Λ. Let $u \in \mathcal{E}'(\mathbb{R}^d_+)$ with $(y,\eta) \in \mathrm{WF}(u)$. If $\eta \in C(y)$, then (y,η) is a visible singularity of u with respect to Λ, and if $\eta \notin \overline{C(x)}$, then (y,η) will be an invisible singularity of u with respect to Λ.

Proof of Proposition 3.10. Let $\eta \in C(y)$. We define $\overline{m} := \eta_1/\eta_3$ and $\overline{n} := \eta_2/\eta_3$, which is possible as η_3 is nonzero. Further, the cutoff function ψ in the definition of the set $C(y)$ is continuous. Thus, there exist $\delta > 0$ and $r > 0$ such that we have

$$\overline{B_r(y)} \subseteq \mathbb{R}^3_+ \quad \text{and} \quad \psi(p,q,x) > 0$$

for $p \in \overline{B_\delta(\overline{m})}$, $q \in \overline{B_\delta(\overline{n})}$, and $x \in \overline{B_r(y)}$.

In case of $\eta_3 > 0$, we define

$$V_\delta(\eta) := \left\{(\lambda m, \lambda n, \lambda)^\top \in \mathbb{R}^3 \,|\, \overline{m} - \delta \leq m \leq \overline{m} + \delta, \overline{n} - \delta \leq n \leq \overline{n} + \delta, \lambda \geq 0\right\},$$

and for $\eta_3 < 0$ we consider

$$V_\delta(\eta) := \left\{(-\lambda m, -\lambda n, -\lambda)^\top \in \mathbb{R}^3 \,|\, \overline{m} - \delta \leq m \leq \overline{m} + \delta, \overline{n} - \delta \leq n \leq \overline{n} + \delta, \lambda \geq 0\right\}.$$

In both cases, $V_\delta(\eta)$ is a conic neighborhood of η.

In the beginning of this section we have seen that nearly all terms of the symbol depend solely on the two ratios p and q. Hence, we introduce the set

$$M := \Big\{(p,q,x) \in \mathbb{R} \times \mathbb{R} \times \mathbb{R}^3_+ \,|\,$$
$$\text{there exists } \xi \in V_\delta(\eta)\backslash\{0\},\ p = \xi_1/\xi_3,\ q = \xi_2/\xi_3 \text{ and } x \in \overline{B_r(y)}\Big\}$$
$$= \left\{(p,q,x) \in \mathbb{R} \times \mathbb{R} \times \mathbb{R}^3_+ \,|\, \overline{m} - \delta \leq p \leq \overline{m} + \delta, \overline{n} - \delta \leq q \leq \overline{n} + \delta, \text{ and } x \in \overline{B_r(y)}\right\},$$

which is obviously closed and bounded and thus a compact subset of $\mathbb{R}^5$.

According to Theorem 3.9 we have

$$\sigma(F^*\psi F) = \frac{(2\pi)^5(D_+(p,q,x)+D_-(p,q,x))^2\psi(s(p,q,x),\varphi(s(p,q,x),x))x_3^2}{D_+(p,q,x)^4 D_-(p,q,x)^4|B(p,q,x)|}\frac{1}{\xi_3^2}$$

for $(p,q,x)\in M$ and ξ_3 such that $\xi\in V_\delta(\eta)\backslash\{0\}$ holds. The map

$$G\colon M\ni(p,q,x)\mapsto\left|\frac{(2\pi)^5(D_+(p,q,x)+D_-(p,q,x))^2\psi(s(p,q,x),\varphi(s(p,q,x),x))x_3^2}{D_+(p,q,x)^4 D_-(p,q,x)^4|B(p,q,x)|}\right|$$

is continuous and attains its positive minimum on M:

$$N_{V_\delta(\eta),r} := \min_{(p,q,x)\in M} G(p,q,x) > 0.$$

Thus,

$$|\sigma(F^*\psi F)(x,\xi)| = |\sigma(F^*\psi F)(p,q,x,\xi_3)| \geq N_{V_\delta(\eta),r}\frac{1}{\xi_3^2}$$

and accordingly

$$|\sigma(\Lambda)(x,\xi)| = |\sigma(-\Delta\partial_3 F^*\psi F)(x,\xi)| \geq N_{V_{\delta(\eta),r}}|\xi|$$

for $x\in\overline{B_r(y)}$ and $\xi\in V_\delta(\eta)\backslash\{0\}$. Finally,

$$|\sigma(\Lambda)(x,\xi)| \geq \frac{1}{2}N_{V_\delta(\eta),r}(1+|\xi|) = C_{\delta,\eta,r}(1+|\xi|)$$

with $C_{\delta,\eta,r} := \frac{1}{2}N_{V_\delta(\eta),r}$ for $x\in B_r(y)$ and $\xi\in V_\delta(\eta)$ with $|\xi|\geq 1$. Hence, Λ is microlocally elliptic of order 1 at (y,η).

The second statement can be validated using Remark 3.3 of [22]. ∎

3.4. Modification of the reconstruction operator. Recall that we identify both Λ and Λ_δ. The following two results are immediate corollaries of Theorem 3.9.

Corollary 3.11. *For zero offset, $\alpha = 0$, we have that*

$$\sigma(\Lambda)(x,\xi) = \frac{16\pi^5\xi_3|\xi_3|\psi\left(x_1-\frac{\xi_1}{\xi_3}x_3, x_2-\frac{\xi_2}{\xi_3}x_3, 2|\xi|\frac{x_3}{\xi_3}\right)}{x_3^2|\xi|}$$

for $x\in\mathbb{R}^3_+$ and $\xi\in\mathbb{R}^3\backslash\{0\}$ with $\xi_3\neq 0$. Further, $\sigma(\Lambda)(x,\xi)=0$ for $x\in\mathbb{R}^3_+$ and $\xi\in\mathbb{R}^3\backslash\{0\}$ with $\xi_3=0$.

Proof. This follows in a straightforward way by evaluating the right-hand side of (3.6) for $\alpha=0$. ∎

Remark 3.12. In this remark we comment on the effect of $C(x)$ on the recoverable part of the wave front set in case $\alpha=0$. Assume that ψ is positive on $S_0\times(t_-,t_+)$ where $S_0=(a_1,b_1)\times(a_2,b_2)$, $a_1<b_1$, $a_2<b_2$, and $0<t_-<t_+$. Then, $\xi\in C(x)$ if and only if

$$\frac{x_i-b_i}{x_3}\leq\frac{\xi_i}{\xi_3}\leq\frac{x_i-a_i}{x_3},\quad i\in\{1,2\};\qquad \frac{t_-}{2x_3}\leq\sqrt{\frac{\xi_1^2}{\xi_3^2}+\frac{\xi_2^2}{\xi_3^2}+1}\leq\frac{t_+}{2x_3}.$$

With increasing depth only elements (x,ξ) of the wave front set can be recovered with dominant vertical directions ξ_3. Also its horizontal position (x_1,x_2) (relative to S_0) affects the recovery of (x,ξ) as an element of the wave front set: For a fixed depth, if (x_1,x_2) is far from S_0, then the horizontal components ξ_1 and ξ_2 will need to be dominant (and t_+ will need to be sufficiently large, of course).

Analogous statements hold for $\alpha>0$ because the geometry of the ellipsoids that determine visible singularities are similar to spheres.

Corollary 3.13. *Let $(x,\xi)\in\mathbb{R}^3_+\times\mathbb{R}^3$ with $\xi_3\neq 0$. Then,*

$$\sigma(\Lambda)(x,\xi)\sim\frac{1}{\alpha^2}\quad \textit{for } \xi_2\neq 0\qquad \textit{and}\qquad \sigma(\Lambda)(x,\xi)\sim\frac{1}{\alpha}\quad \textit{for } \xi_2=0$$

where "$\sim$" denotes asymptotic equality for $\alpha\to\infty$.

Proof. First, we start with $\xi_2\neq 0$. We separately consider the two cases that ξ_2 and ξ_3 have the same and opposite signs. For each case we obtain limits of ω, B, and αA as $\alpha\to\infty$. From this we can deduce that $\alpha^2\sigma(\Lambda)(x,\xi)$ has a limit as well for $\alpha\to\infty$. The necessary calculations are lengthy and tedious; see [10, Cor. 3.29] for full details.

If $\xi_2=0$, then a direct calculation yields

$$\sigma(\Lambda)(x,\xi)=\frac{16\pi^5|\xi|\psi\Big(x_1-\frac{\xi_1}{\xi_3},x_2,\varphi\Big(x_1-\frac{\xi_1}{\xi_3},x_2,x\Big)\Big)}{x_3^2\xi_3\sqrt{\frac{\alpha^2}{x_3^2}+\frac{\xi_1^2}{\xi_3^2}+1}\Big(\frac{\xi_1^2}{\xi_3^2}+1\Big)},$$

which behaves like $1/\alpha$. ∎

Hence, the ellipticity of Λ deteriorates for large α^2/x_3 and for large x_3/α.

Based on the observations of the last two corollaries, we modify Λ introducing

$$\Lambda_{\mathrm{mod},0}:=-\Delta\partial_3 MF^*\psi F, \tag{3.9}$$

$$\Lambda_{\mathrm{mod},i}:=-\Delta\partial_3(M+\alpha^i\,\mathrm{Id})F^*\psi F\qquad \text{for } i\in\{1,2\}, \tag{3.10}$$

where M is the multiplication operator by x_3^2. Their top order symbols are

$$\sigma(\Lambda_{\mathrm{mod},0})(x,\xi)=x_3^2\,\sigma(\Lambda)(x,\xi),\quad \sigma(\Lambda_{\mathrm{mod},i})(x,\xi)=(x_3^2+\alpha^i)\sigma(\Lambda)(x,\xi)\quad \text{for } i\in\{1,2\}.$$

The microlocal ellipticity of the latter two remains unaffected to some extent for large α^2/x_3 and large x_3/α. Furthermore, Proposition 3.10 holds unchanged for the three new operators.

4. Approximate inverse and reconstruction kernels. Our numerical algorithm to compute Λn from the data y given in (2.5) is based on the regularization scheme of approximate inverse [16] because the structure of Λ and its modifications fit perfectly. Instead of Λn we will recover a smoothed version $\Lambda n\star e$ where e is a mollifier, that is, a smooth approximation of the Dirac distribution.

We work with the following family of mollifiers [11]: For $p\in\mathbb{R}^3_+$ and $\gamma,k>0$ let

$$e_{p,\gamma,k}(x)=C_{\gamma,k}\begin{cases}\big(\gamma^2-|x-p|^2\big)^k, & |x-p|<\gamma,\\ 0, & |x-p|\geq\gamma,\end{cases}\qquad x\in\mathbb{R}^3_+,$$

with the normalization constant

$$C_{\gamma,k} = \left(\int_{B_\gamma(p)} \left(\gamma^2 - |x-p|^2\right)^k \, \mathrm{d}x \right)^{-1} = \frac{\Gamma(k+5/2)}{\pi^{3/2}\gamma^{2k+3}\Gamma(k+1)}.$$

The region of integration is $B_\gamma(p)$, the ball of radius γ about p. We have $\operatorname{supp} e_{p,\gamma,k} = \overline{B_\gamma(p)}$ and $\int_{\mathbb{R}^3} e_{p,\gamma,k}(x)\,\mathrm{d}x = 1$. Thus, $e_{p,\gamma,k} \to \delta(\cdot - p)$ for $\gamma \to 0$. Here, the parameter γ is a scaling/regularization parameter and k determines the smoothness of $e_{p,\gamma,k}$.

We approximate Λn at p for $n \in \mathcal{E}'(\mathbb{R}^3_+)$ now by

$$L_\gamma n(p) := \langle \Lambda n, e_{p,\gamma,k} \rangle = \langle -\Delta \partial_3 F^* \psi F n, e_{p,\gamma,k} \rangle = \langle \psi F n, F \partial_3 \Delta e_{p,\gamma,k} \rangle, \tag{4.1}$$

where $\langle \cdot, \cdot \rangle$ denotes the usual extension of the L^2 inner product.

Next, we replace Fn by the data y stated in (2.5) and obtain

$$L_\gamma n(p) = \langle \psi y, r_{p,\gamma,k} \rangle = \int_{S_0 \times (2\alpha,\infty)} \psi(s,t) y(s,t)\, r_{p,\gamma,k}(s,t)\, \mathrm{d}(s,t)$$

with the reconstruction kernel

$$r_{p,\gamma,k} := F \partial_3 \Delta e_{p,\gamma,k},$$

which is independent of the data and needs to be precomputed. In what follows, let m_3 be the monomial function $\mathrm{m}_3(x) = x_3$ for $x \in \mathbb{R}^3$.

Lemma 4.1. *Let $\gamma > 0$ and $k \geq 3$. With $\widetilde{e}_{p,\gamma,k} = e_{p,\gamma,k}/C_{\gamma,k}$ we have*

$$\begin{aligned} r_{p,\gamma,k}(s,t) = 4k(k-1)C_{\gamma,k}\Big(& 5F\big(\mathrm{m}_3(\cdot - p)\, \widetilde{e}_{p,\gamma,k-2}\big) \\ & - 2(k-2)F\big(\mathrm{m}_3(\cdot - p)\, |\cdot - p|^2\, \widetilde{e}_{p,\gamma,k-3}\big)\Big)(s,t) \end{aligned}$$

for $(s,t) \in S_0 \times (2\alpha, \infty)$.

Proof. A straightforward calculation yields first

$$\Delta \widetilde{e}_{p,\gamma,k}(x) = -6k\left(\gamma^2 - |x-p|^2\right)^{k-1} + 4k(k-1)|x-p|^2\left(\gamma^2 - |x-p|^2\right)^{k-2} \chi_{B_\gamma(p)}(x)$$

and then

$$\begin{aligned} \partial_3 \Delta \widetilde{e}_{p,\gamma,k}(x) = \Big(& 20k(k-1)(x_3 - p_3)\left(\gamma^2 - |x-p|^2\right)^{k-2} \\ & - 8k(k-1)(k-2)(x_3 - p_3)|x-p|^2\left(\gamma^2 - |x-p|^2\right)^{k-3}\Big)\chi_{B_\gamma(p)}(x). \end{aligned}$$

The assertion follows from $e_{p,\gamma,k} = C_{\gamma,k}\widetilde{e}_{p,\gamma,k}$. ∎

Analogously, we define the approximations

$$L_{\gamma,\mathrm{mod},i} n(p) := \langle \Lambda_{\mathrm{mod},i} n, e_{p,\gamma,k} \rangle = \langle \psi F n, r_{p,\gamma,k,\mathrm{mod},i} \rangle \quad \text{for } i \in \{0,1,2\} \tag{4.2}$$

with the corresponding kernels

$$r_{p,\gamma,k,\mathrm{mod},0} := FM\partial_3 \Delta e_{p,\gamma,k} \quad \text{and} \quad r_{p,\gamma,k,\mathrm{mod},i} := F(M + \alpha^i \,\mathrm{Id})\partial_3 \Delta e_{p,\gamma,k},\ i \in \{1,2\}.$$

Corollary 4.2. *Let $\gamma > 0$, $k \geq 3$, and $\widetilde{e}_{p,\gamma,k}$ be as in Lemma 4.1. Then, for $(s,t) \in S_0 \times (2\alpha, \infty)$,*

$$r_{p,\gamma,k,\mathrm{mod},0}(s,t) = 4k(k-1)C_{\gamma,k}\Big(5F\big(\mathrm{m}_3(\cdot - p)\,\mathrm{m}_3^2\,\widetilde{e}_{p,\gamma,k-2}\big) - 2(k-2)F\big(\mathrm{m}_3(\cdot - p)\,\mathrm{m}_3^2\,|\cdot - p|^2\,\widetilde{e}_{p,\gamma,k-3}\big)\Big)(s,t)$$

and

$$r_{p,\gamma,k,\mathrm{mod},i}(s,t) = r_{p,\gamma,k,\mathrm{mod},0}(s,t) + \alpha^i\, r_{p,\gamma,k}(s,t),\ i \in \{1,2\}.$$

4.1. The elliptic Radon transform of a characteristic function supported in a ball. For the computation of the reconstruction kernels according to the above lemma and corollary we have to apply F to functions which are supported in a ball $B_r(P)$ for $P = (p_1, p_2, p_3) \in \mathbb{R}^3_+$ and $0 < r < p_3$.

Let $n \in L^2(\mathbb{R}^3_+)$ with $\mathrm{supp}(n) \subseteq B_r(P)$. Using the ellipsoids of the Radon transform, this situation is illustrated in Figure 1, where n vanishes outside the ball $B_r(P)$.

To calculate Fn, we first shift the coordinate system (x_1, x_2, x_3) such that $(s_1, s_2, 0)^\top$ is the new origin. Afterward, we rotate the system in such a way that P lies in the $x_2' - x_3'$-plane in the coordinate system (x_1', x_2', x_3'). This rotation R is given by the following matrix:

$$R = \begin{pmatrix} \cos(\beta) & 0 & -\sin(\beta) \\ 0 & 1 & 0 \\ \sin(\beta) & 0 & \cos(\beta) \end{pmatrix}, \quad \beta = \arctan((p_1 - s_1)/p_3).$$

Using the notation $\mathbf{s} := (s,0)^\top = (s_1, s_2, 0)^\top$, we calculate

$$\begin{aligned} Fn(s,t) &= \int_{\mathbb{R}^3_+} n(x)A(s,x)\delta(t - \varphi(s,x))\,\mathrm{d}x = \int_{\mathbb{R}^3} n(x)A(s,x)\chi_{B_r(P)}(x)\delta(t - \varphi(s,x))\,\mathrm{d}x \\ &= \int_{\mathbb{R}^3} n(R^{-1}x + \mathbf{s})A((0,0),x)\chi_{B_r(P')}(x)\delta(t - \varphi((0,0),x))\,\mathrm{d}x, \end{aligned}$$

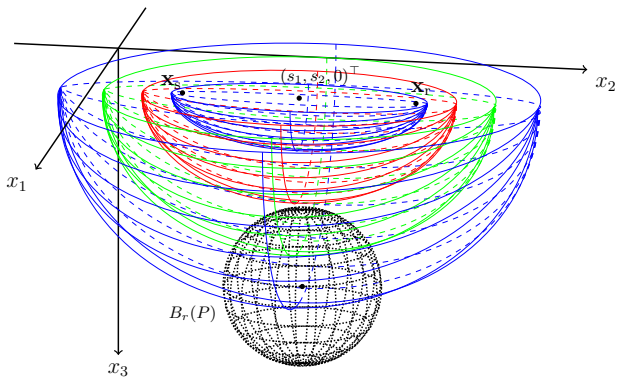

Figure 1. *The given situation for several travel times t, respectively. Each travel time t is associated with one open half ellipsoid for fixed $s \in S_0$.*

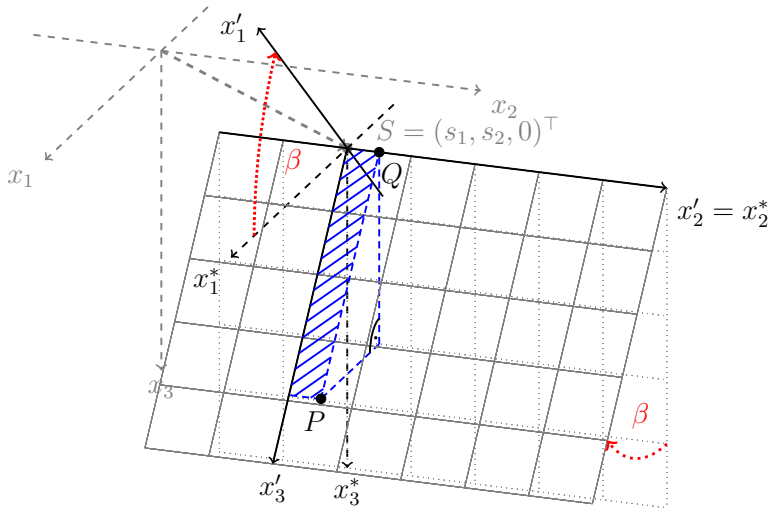

Figure 2. *The shift into the coordinate system (x_1^*, x_2^*, x_3^*), and afterward, the rotation into the new coordinate system (x_1', x_2', x_3') such that $(s_1, s_2, 0)^\top$ is the origin and P lies in the x_2'-x_3'-plane. Here, the point Q is given by $(0, p_2', 0)^\top$.*

where

$$P' = (0, p_2', p_3') = R(P - \mathbf{s}) = \left(0, p_2 - s_2, \frac{p_3}{\cos\left(\arctan\left(\frac{p_1 - s_1}{p_3}\right)\right)}\right)^\top.$$

The last component p_3' of P' is calculated with the help of two trigonometric relations in a suitable right triangle in the $x_2' = p_2'$-plane; see Figure 2. Next, we introduce the prolate spheroidal coordinates in $\mathbb{R}^3$, which are realized by $x = x(s, t, \phi, \theta)$ with components

$$\begin{aligned} x_1 &= s_1 + \sqrt{\frac{1}{4}t^2 - \alpha^2}\sin(\phi)\cos(\theta), \\ x_2 &= s_2 + \frac{1}{2}t\cos(\phi), \\ x_3 &= \sqrt{\frac{1}{4}t^2 - \alpha^2}\sin(\phi)\sin(\theta), \end{aligned} \tag{4.3}$$

for $t > 2\alpha$, $\phi \in (0, \pi)$, and $\theta \in (0, 2\pi)$. These coordinates fit to prolate spheroids, i.e., rotational ellipsoids with two half axes having the same length and a longer third one, which is the rotational axis. Such ellipsoids are just given by $t = \varphi(s, x)$ for $x \in \mathbb{R}^3$. The variable t is the travel time, the angle θ is the rotational angle, and the foci are $(s_1, s_2 - \alpha, 0)^\top$ and $(s_1, s_2 + \alpha, 0)^\top$. The different angles of θ are arranged concentrically, whereas the angles ϕ are located in hyperbolic orbits.

Since we consider the situation in the new coordinate system (x_1', x_2', x_3'), we set $s_1 = s_2 = 0$ and so the ellipsoids we consider have the two foci $(0, -\alpha, 0)^\top$ and $(0, \alpha, 0)^\top$. Hence, we write $x = x(0, t, \phi, \theta) = x(t, \phi, \theta)$ and obtain

$$Fn(s, t) = \frac{1}{2}\int_{\theta_{\min}}^{\theta_{\max}} \int_{\phi(\theta)_{\min}}^{\phi(\theta)_{\max}} n(R^{-1}x(t, \phi, \theta) + \mathbf{s})\chi_{B_r(P')}(x(t, \phi, \theta))\sin(\phi)\,\mathrm{d}\phi\,\mathrm{d}\theta, \tag{4.4}$$

where $\theta_{\min}$ and $\theta_{\max}$ are defined by

$$\theta_{\min\,/\,\max} = \theta_{\min\,/\,\max}(t) := \min\,/\,\max\{\theta \in [0, 2\pi) \,|\, x(t, \phi, \theta) \in \overline{B_r(P')},\ \phi \in [0, \pi)\}$$

for fixed $t \in (2\alpha, \infty)$. Further, $\phi(\theta)_{\min}$ and $\phi(\theta)_{\max}$ are given by

$$\phi(\theta)_{\min\,/\,\max} = \phi(\theta, t)_{\min\,/\,\max} := \min\,/\,\max\{\phi \in [0, \pi) \,|\, x(t, \phi, \theta) \in \overline{B_r(P')}\}$$

for fixed $\theta \in (\theta_{\min}, \theta_{\max})$ and $t \in (2\alpha, \infty)$.

Before we go into further details regarding these four angles, we limit the interval $(2\alpha, \infty)$ of the travel time t. In the new coordinate system the considered ellipsoids have the two foci $(0, -\alpha, 0)^\top$ and $(0, \alpha, 0)^\top$. As in the original situation illustrated in Figure 1, these ellipsoids intersect $B_r(P)$ only for travel times t in a bounded interval. The minimal and maximal values are

$$T_{\min} := \min_{y \in C} \left(|(0, -\alpha, 0)^\top - y| + |y - (0, \alpha, 0)^\top| \right)$$

and

$$T_{\max} := \max_{y \in C} \left(|(0, -\alpha, 0)^\top - y| + |y - (0, \alpha, 0)^\top| \right),$$

where C is the circle which is the intersection of the $x_2' - x_3'$-plane with the boundary of the ball $B_r(P')$. So, we have $Fn(s, t) = 0$ for $s \in S_0$ and $t \le T_{\min}$ or $t \ge T_{\max}$. All further details can be found in [10, sect. 4.2.4].

Now, we sketch how to obtain the four angles limiting the integrals. In case of $\theta_{\min}$ and $\theta_{\max}$ we consider the plane $x_2 = p_2'$. We are thus in a two-dimensional setting, in which $\theta_{\min}$ and $\theta_{\max}$ are the two angles of θ in prolate spheroidal coordinates enclosing the associated cross section of the ball $B_r(P')$. An illustration is given in the left image of Figure 3. For the calculation of $\theta_{\min}$ and $\theta_{\max}$ we determine the angle $\vartheta_{\max}$ marked in Figure 3 and use the symmetry with respect to $\theta = \pi/2$; see [10, sect. 4.2.3] for exhaustive explanations.

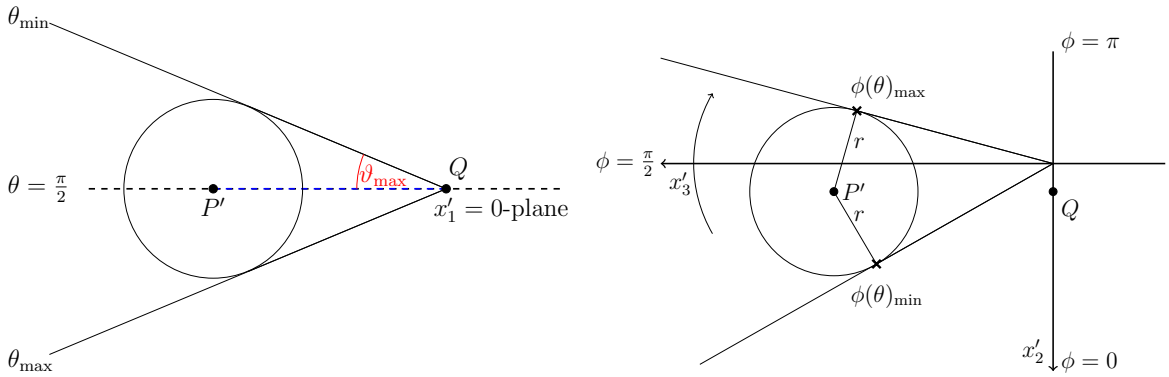

Figure 3. *Left: An illustration of $\theta_{\min}$ and $\theta_{\max}$ in the $x_2' = p_2'$-plane. Right: The angles $\phi(\theta)_{\min}$ and $\phi(\theta)_{\max}$ marked in the $x_1' = 0$-plane from a bird's eye view.*

To get $\phi(\theta)_{\min}$ and $\phi(\theta)_{\max}$, we fix $\theta \in [\theta_{\min}, \theta_{\max}]$. The angles $\phi(\theta)_{\min}$ and $\phi(\theta)_{\max}$ are given by the minimal and maximal angles of ϕ corresponding to the points on $\partial B_r(P')$ for fixed $\theta \in (\theta_{\min}, \theta_{\max})$ as illustrated in the right image of Figure 3. Thus, we have to solve the equation

$$r^2 = |P' - x(t, \phi(\theta), \theta)|^2$$

for $\phi(\theta)$ in our new coordinate system (x_1', x_2', x_3'). By the definition of the prolate spheroidal coordinates this equation has exactly two solutions $\phi(\theta)$ in $[0, \pi)$. Next, we insert these coordinates setting $s_1 = s_2 = 0$ in (4.3) and get, using the substitution $z = \cos(\phi(\theta))$, the following identity:

$$r^2 = (p_2')^2 + (p_3')^2 + \frac{1}{4}t^2 - \alpha^2(1 - z^2) - p_2' t z - p_3' \sqrt{t^2 - 4\alpha^2}\sqrt{1 - z^2}\sin(\theta).$$

Solving this equation and resubstitution yield two solutions z_1 and z_2 in $[-1, 1]$. Without loss of generality, we obtain

$$\phi(\theta)_{\min} = \arccos(z_1) \quad \text{and} \quad \phi(\theta)_{\max} = \arccos(z_2)$$

with $\phi(\theta)_{\min} < \phi(\theta)_{\max}$. In our implementation we obtain z_1 and z_2 approximately by Newton's method.

4.2. The elliptic Radon transform of the characteristic function of a half space. For our numerical experiments in the next section we provide Fn where n is the characteristic function of a half space, i.e., $n = \chi_{\{x \in \mathbb{R}^3_+ \,|\, x_3 \geq l\}}$ for some $l > 0$. We directly work in prolate spheroidal coordinates (4.3), this time with arbitrary s_1, s_2 and restricted to $\mathbb{R}^3_+$, i.e., $t \in (2\alpha, \infty)$, $\phi \in [0, \pi)$, and $\theta \in [0, \pi)$. Hence, by $x = x(s, t, \phi, \theta)$,

$$Fn(s,t) = \frac{1}{2}\int_{\theta_{\min}}^{\theta_{\max}} \int_{\phi(\theta)_{\min}}^{\phi(\theta)_{\max}} n(x(s,t,\phi,\theta))\sin(\phi)\,\mathrm{d}\phi\,\mathrm{d}\theta$$

for $(s, t) \in S_0 \times (2\alpha, \infty)$ with

$$\theta_{\min\,/\,\max} = \theta_{\min\,/\,\max}(s,t) := \min\,/\,\max\{\theta \in [0,\pi) \,|\, x(s,t,\phi,\theta) \in \operatorname{supp}(n), \phi \in [0,\pi)\}$$

and

$$\phi(\theta)_{\min\,/\,\max} := \phi(\theta)_{\min\,/\,\max}(s,t) \;:= \min\,/\,\max\{\phi \in [0,\pi) \,|\, x(s,t,\phi,\theta) \in \operatorname{supp}(n)\}.$$

We have $n(x(s, t, \phi, \theta)) = 1$ for $\theta \in (\theta_{\min}, \theta_{\max})$ and $\phi(\theta) \in (\phi(\theta)_{\min}, \phi(\theta)_{\max})$. Otherwise, $n(x(s, t, \phi, \theta)) = 0$. Therefore,

$$Fn(s,t) = \frac{1}{2}\int_{\theta_{\min}}^{\theta_{\max}} \int_{\phi(\theta)_{\min}}^{\phi(\theta)_{\max}} \sin(\phi)\,\mathrm{d}\phi\,\mathrm{d}\theta, \quad (s,t) \in S_0 \times (2\alpha, \infty). \tag{4.5}$$

We obtain the four required angles from the points of intersection marked with a cross in Figure 4. For $\theta_{\min}$ and $\theta_{\max}$ we consider the plane $x_2 = s_2$ where $\phi = \pi/2$ according to (4.3). As $x_3 = l$ for the points in Figure 4, we need to solve $l = x_3 = \sqrt{\frac{1}{4}t^2 - \alpha^2}\sin(\theta)$ for θ yielding

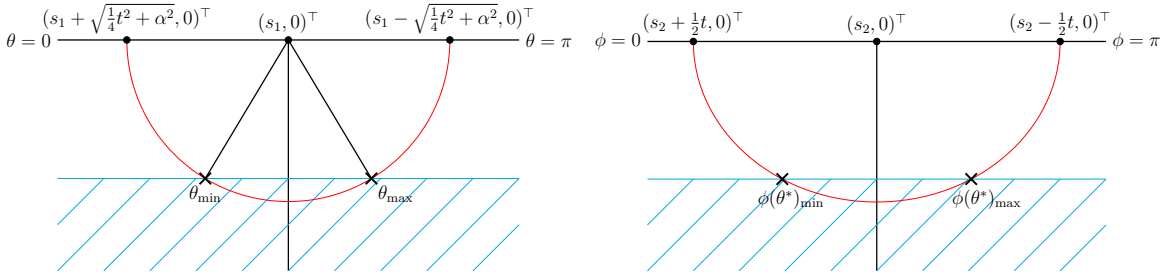

Figure 4. *Left: The minimal and maximal possible angles for θ illustrated in the $x_2 = s_2$-plane. Right: In the $\theta = \theta^*$-plane we consider the angles $\phi(\theta^*)_{\min}$ and $\phi(\theta^*)_{\max}$, which are determined by the coordinates of the two marked points.*

$$\theta_{\min} = \arcsin\left(\frac{l}{\sqrt{\frac{1}{4}t^2-\alpha^2}}\right) \quad \text{and} \quad \theta_{\max} = \pi - \theta_{\min}.$$

Similar reasoning leads to $\phi(\theta)_{\min}$ and $\phi(\theta)_{\max}$ for $\theta^* \in [\theta_{\min}, \theta_{\max}]$. We consider the plane $\theta = \theta^*$ illustrated on the right in Figure 4. Here, the equation is $l = \sqrt{\frac{1}{4}t^2-\alpha^2}\sin(\phi(\theta^*))\sin(\theta^*)$, which is solved by

$$\phi(\theta^*)_{\min} = \arcsin\left(\frac{l}{\sqrt{\frac{1}{4}t^2-\alpha^2}\sin(\theta^*)}\right) \quad \text{and} \quad \phi(\theta^*)_{\max} = \pi - \phi(\theta^*)_{\min}.$$

If the travel time t is too small, then the ellipsoids do not intersect the half space. The limiting travel time is given by $T_{\min} = \min_{\{x\in\mathbb{R}^3_+ \,|\, \varphi(s,x)=t\}}(|\mathbf{x}_s(s)-x|+|x-\mathbf{x}_r(s)|)$. Obviously, the minimum is attained at $x = (s_1, s_2, l)$ with minimal value $T_{\min} = 2\sqrt{\alpha^2+l^2}$. Thus, $Fn(s,t) = 0$ for $t \le T_{\min}$ and $s \in S_0$.

4.3. Computation of the reconstruction kernels. By the representation of $r_{p,\gamma,3}$ in Lemma 4.1 and the results of section 4.1 we have

$$\begin{aligned}
&r_{p,\gamma,3}(s,t)\\
&\quad= C_{\gamma,3}\frac{1}{2}\int_{\theta_{\min}}^{\theta_{\max}}\int_{\phi(\theta)_{\min}}^{\phi(\theta)_{\max}}\Big(120\gamma^2\Big([R^{-1}x(t,\phi,\theta)+(s_1,s_2,0)^\top]_3-p_3\Big)\\
&\qquad-168\Big([R^{-1}x(t,\phi,\theta)+(s_1,s_2,0)^\top]_3-p_3\Big)\Big|R^{-1}x(t,\phi,\theta)+(s_1,s_2,0)^\top-p|^2\Big)\\
&\qquad\times\chi_{B_\gamma(p')}(x(t,\phi,\theta))\sin(\phi)\,\mathrm{d}\phi\,\mathrm{d}\theta\\
&\quad= \frac{315}{64\pi\gamma^9}\frac{1}{2}\int_{\theta_{\min}}^{\theta_{\max}}\int_{\phi(\theta)_{\min}}^{\phi(\theta)_{\max}}\Bigg(120\gamma^2(-\sin(\beta)\cos(\theta)+\cos(\beta)\sin(\theta))\sqrt{\frac{1}{4}t^2-\alpha^2}\sin^2(\phi)\\
&\qquad-120\gamma^2p_3\sin(\phi)\\
&\qquad-168(-\sin(\beta)\cos(\theta)+\cos(\beta)\sin(\theta))\sqrt{\frac{1}{4}t^2-\alpha^2}|\,x(t,\phi,\theta)-p'|^2\sin^2(\phi)\\
&\qquad+168p_3|\,x(t,\phi,\theta)-p'|^2\sin(\phi)\Bigg)\chi_{B_\gamma(p')}(x(t,\phi,\theta))\,\mathrm{d}\phi\,\mathrm{d}\theta
\end{aligned}$$

for $(s,t) \in S_0 \times (T_{\min}, T_{\max})$. Further,

$$|x(t,\phi,\theta) - p'|^2 = (a + b\sin(\phi))^2 + (c + d\cos(\phi))^2 + (e + f\sin(\phi))^2, \tag{4.6}$$

where

$$a = -p_1' = 0, \qquad b = \sqrt{\frac{1}{4}t^2 - \alpha^2}\cos(\theta), \qquad c = -p_2' = -p_2 + s_2,$$
$$d = \frac{1}{2}t, \qquad e = -p_3' = -\frac{p_3}{\cos\left(\arctan\left(\frac{p_1 - s_1}{p_3}\right)\right)}, \qquad f = \sqrt{\frac{1}{4}t^2 - \alpha^2}\sin(\theta),$$

for $t \in (T_{\min}, T_{\max})$, $\phi \in [0,\pi)$, and $\theta \in [0, 2\pi)$. Hence, to compute numerical values for $r_{p,\gamma,3}$, we need the antiderivatives of the following functions:

$$\phi \mapsto \sin^2(\phi), \qquad \phi \mapsto (a + b\sin(\phi))^2 + (c + d\cos(\phi))^2 + (e + f\sin(\phi))^2\sin^2(\phi),$$
$$\phi \mapsto \sin(\phi), \qquad \phi \mapsto (a + b\sin(\phi))^2 + (c + d\cos(\phi))^2 + (e + f\sin(\phi))^2\sin(\phi).$$

As these four functions are trigonometric polynomials in ϕ, their antiderivatives exist in closed form. We found analytic expressions by a computer algebra system and imported them in our code.

Analogously,

$$\begin{aligned}
&r_{p,\gamma,3,\mathrm{mod},0}(s,t) \\
&\quad = \frac{315}{64\pi\gamma^9}\frac{1}{2}\int_{\theta_{\min}}^{\theta_{\max}}\int_{\phi(\theta)_{\min}}^{\phi(\theta)_{\max}} \Bigg(120\gamma^2(-\sin(\beta)\cos(\theta) + \cos(\beta)\sin(\theta))^3 \\
&\qquad \times \left(\sqrt{\frac{1}{4}t^2 - \alpha^2}\right)^3 \sin^4(\phi) \\
&\qquad - 120\gamma^2 p_3(-\sin(\beta)\cos(\theta) + \cos(\beta)\sin(\theta))^2 \left(\sqrt{\frac{1}{4}t^2 - \alpha^2}\right)^2 \sin^3(\phi) \\
&\qquad - 168(-\sin(\beta)\cos(\theta) + \cos(\beta)\sin(\theta))^3 \left(\sqrt{\frac{1}{4}t^2 - \alpha^2}\right)^3 |x(t,\phi,\theta) - p'|^2 \sin^4(\phi) \\
&\qquad + 168p_3(-\sin(\beta)\cos(\theta) + \cos(\beta)\sin(\theta))^2 \left(\sqrt{\frac{1}{4}t^2 - \alpha^2}\right)^2 |x(t,\phi,\theta) - p'|^2 \sin^3(\phi) \Bigg) \\
&\qquad \times \chi_{B_\gamma(p')}(x(t,\phi,\theta))\,\mathrm{d}\phi\,\mathrm{d}\theta.
\end{aligned}$$

In view of (4.6) we now need the antiderivatives of

$$\phi \mapsto \sin^4(\phi), \qquad \phi \mapsto (a + b\sin(\phi))^2 + (c + d\cos(\phi))^2 + (e + f\sin(\phi))^2\sin^4(\phi),$$
$$\phi \mapsto \sin^3(\phi), \qquad \phi \mapsto (a + b\sin(\phi))^2 + (c + d\cos(\phi))^2 + (e + f\sin(\phi))^2\sin^3(\phi),$$

which we obtain analytically as before.

Knowing $r_{p,\gamma,3}$ and $r_{p,\gamma,3,\mathrm{mod},0}$ means knowing $r_{p,\gamma,k,\mathrm{mod},1}$ and $r_{p,\gamma,k,\mathrm{mod},2}$ as well due to Corollary 4.2. All in all, we have the explicit expressions of the different reconstruction kernels at a point $(s,t) \in S_0 \times (2\alpha,\infty)$ depending on the limiting angles $\theta_{\min}$, $\theta_{\max}$, $\phi_{\min}(\theta)$, and $\phi_{\max}(\theta)$ and the travel times $T_{\min}$ and $T_{\max}$.

5. Numerical experiments. For the numerical examples we have to evaluate integrals of the form

$$\widetilde{L}_\gamma n(p) = \langle \psi y, \widetilde{r}_{p,\gamma,3} \rangle = \int_{S_0 \times (2\alpha,\infty)} \psi(s,t) y(s,t) \widetilde{r}_{p,\gamma,3}(s,t)\, \mathrm{d}(s,t)$$

for $p \in \mathbb{R}^3_+$ where y is the given data and $\widetilde{r}_{p,\gamma,3}$ represents one of the kernels belonging to the four imaging operators Λ, $\Lambda_{\mathrm{mod},i}$, $i \in \{0,1,2\}$. Further, the cutoff function $\psi \in C_c^\infty(S_0 \times (2\alpha,\infty))$ is taken from [22, sect. 5]: For $\overline{S} > 0$ and $\overline{T} > \underline{T} > 0$ we set

$$\psi(s,t) = \psi(s_1,s_2,t) = \Psi_1(s_1)\Psi_1(s_2)\Psi_2(t), \tag{5.1}$$

where

$$\Psi_1(s) = \begin{cases} 1 & \text{for} \quad |s| < \overline{S}, \\ h(|s|,\overline{S}) & \text{for} \quad \overline{S} \le |s| \le \overline{S}+1, \\ 0 & \text{for} \quad \overline{S}+1 < |s|, \end{cases}$$

and

$$\Psi_2(t) = \begin{cases} 0 & \text{for} \quad t \le \underline{T}, \\ g(t,\underline{T}) & \text{for} \quad \underline{T} < t < 2\underline{T}, \\ 1 & \text{for} \quad 2\underline{T} \le t \le \overline{T}, \\ h(t,\overline{T}) & \text{for} \quad \overline{T} < t < \overline{T}+1, \\ 0 & \text{for} \quad \overline{T}+1 \le t. \end{cases}$$

Using

$$f(r) = \begin{cases} \exp(-\frac{1}{r}) & \text{for} \quad 0 < r, \\ 0 & \text{for} \quad r \le 0, \end{cases}$$

the functions g and h are defined as follows:

$$g(t,\underline{T}) = \frac{f(\frac{t}{\underline{T}}-1)}{f(\frac{t}{\underline{T}}-1)+f(2-\frac{t}{\underline{T}})}, \qquad h(t,\overline{T}) = \frac{f(\overline{T}+1-t)}{f(\overline{T}+1-t)+f(t-\overline{T}-\frac{1}{2})}.$$

Then,

$$\mathrm{supp}(\psi) \subseteq [-\overline{S}-1,\overline{S}+1] \times [\underline{T},\overline{T}+1] \quad \text{and} \quad \psi_{|_{[-\overline{S},\overline{S}]\times[2\underline{T},\overline{T}]}} = 1.$$

In our numerical experiments we assume to know the data y at the uniformly distributed values $(s_1^{(i)}, s_2^{(j)}, t^{(k)}) \in [-s_{\max}, s_{\max}]^2 \times [t_{\min}, t_{\max}]$, $i,j \in \{1,\dots N_s\}$, $k \in \{1,\dots,N_t\}$, where

$s_{\max} > 0$, $t_{\max} > t_{\min} > 2\alpha$, and $N_s, N_t \in \mathbb{N}$. The respective step sizes are $h_s = 2s_{\max}/N_s$ and $h_t = (t_{\max} - t_{\min})/N_t$. Further, $\overline{S} = s_{\max} - 1$, $\underline{T} = t_{\min}$, and $\overline{T} = t_{\max} - 1$.

Since the kernel vanishes for travel times below $T_{\min} = T_{\min}(s_1^{(i)}, s_2^{(j)}, \gamma, p)$ and above $T_{\max} = T_{\max}(s_1^{(i)}, s_2^{(j)}, \gamma, p)$ (see section 4.1), we can restrict the $t^{(k)}$'s to the interval

$$\mathcal{T}_{i,j}(\gamma, p) := \left(T_{\min}\left(s_1^{(i)}, s_2^{(j)}, \gamma\right), T_{\max}\left(s_1^{(i)}, s_2^{(j)}, \gamma\right)\right).$$

Thus, we approximate $\widetilde{L}_\gamma$ straightforwardly by the quadrature rule

$$\mathrm{Q}\,\widetilde{L}_\gamma n(p) := h_t h_s^2 \sum_{i,j=1}^{N_s} \sum_{t^{(k)} \in \mathcal{T}_{i,j}(\gamma,p)} \psi\left(s_1^{(i)}, s_2^{(j)}, t^{(k)}\right) y\left(s_1^{(i)}, s_2^{(j)}, t^{(k)}\right) \times \widetilde{r}_{p,\gamma,3}\left(s_1^{(i)}, s_2^{(j)}, t^{(k)}\right). \tag{5.2}$$

In order not to overload the notation, we refrain from specifying all parameters on which Q depends. Below we will write $\mathrm{Q}\,L_\gamma$ and $\mathrm{Q}\,L_{\gamma,\mathrm{mod},i}$, $i \in \{0,1,2\}$, to indicate which operator (kernel) is actually used in (5.2); compare (4.1) and (4.2).

5.1. Reconstructions from consistent data. For the first set of numerical experiments we choose the function n to be reconstructed as

$$n = \chi_{B_2(0,0,4)} - \chi_{B_1(0,0,4)} + \chi_{B_{1.5}(3,0,5)} + \chi_{\{x_3 \geq 6.5\}};$$

see Figure 5. We generate the data y numerically by evaluating Fn as we have demonstrated in the previous section.

First, we discuss which features of n we expect to see in $\widetilde{L}_\gamma n$. This discussion applies to all four instances of $\widetilde{L}_\gamma$ as all underlying imaging operators enjoy the same order and the

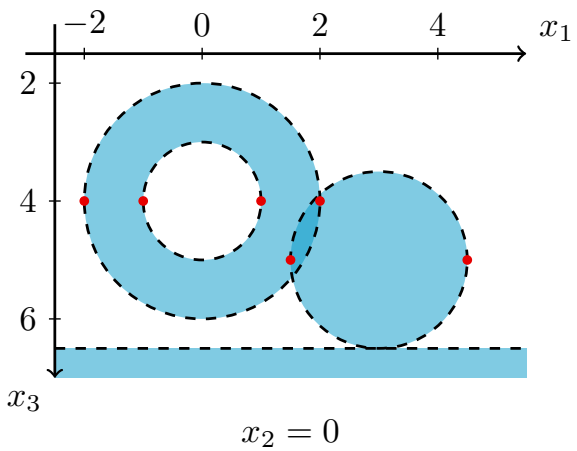

Figure 5. *Cross section of the function n for $x_2 = 0$. On the darker blue area, where the two large circles overlap, n is equal to 2 and on the light blue area to 1, and off the blue areas it is 0. The singularities marked in red are not emphasized independent of the choice of S_0 and ψ. This is because the third component of their normal directions is zero (see Theorem 3.9).*

same decisive microlocal properties. Indeed, let $\widetilde{\Lambda} \in \{\Lambda, \Lambda_{\mathrm{mod},i} \,|\, i \in \{0,1,2\}\}$. Then, $\widetilde{\Lambda}$ is microlocally elliptic of order 1 at $(x_*, \xi_*) \in \mathbb{R}^3_+ \times \mathbb{R}^3 \backslash \{0\}$ if

$$\xi_* \in C(x_*) = \{\xi \in \mathbb{R}^3 \,|\, \xi_3 \neq 0, \psi(s(x_*, \xi), \varphi(s(x_*, \xi), x_*)) > 0\}$$

(see Proposition 3.10). Hence, by Theorem 3.6,

$$(x_*, \xi_*) \in \mathrm{WF}^{-1/2}(\widetilde{\Lambda} n) \quad \text{for } (x_*, \xi_*) \in \mathrm{WF}(n) = \mathrm{WF}^{1/2}(n). \tag{5.3}$$

This means that if the third component of the normal ξ_* at an element x_* of the singular support of n does not vanish and if $\psi(x_*) > 0$, then the Sobolev smoothness of $\widetilde{\Lambda} n(x_*)$ drops by one order in direction ξ_*. More precisely, the smoothness decreases from $H^{1/2}$ to $H^{-1/2}$.

Recall that

$$\mathrm{WF}(\widetilde{\Lambda} n) \subseteq \mathrm{WF}(F^* \psi F n) \tag{5.4}$$

by the pseudolocal property of Theorem 3.5. Further, $(x, \xi) \in \mathrm{WF}(F^* \psi F n)$ only if there exists $s \in S_0$ and $\omega \neq 0$ such that $\xi = \omega \nabla_x \varphi(s, x)$; see Theorem 3.8. Since the set S_0 is bounded in applications, there will be pairs (x, ξ) for which no $s \in S_0$ and $\omega \neq 0$ exist. These singularities and those for which $\xi \notin \overline{C(x)}$ (see Proposition 3.10 and Remark 3.12) will not be preserved; they are invisible singularities with respect to $\widetilde{\Lambda}$ (see Definition 3.7). For instance, the red points in Figure 5 are invisible for any choice of S_0 and ψ.

In what follows, we provide the approximations $\mathrm{Q}\, L_\gamma n$, $\mathrm{Q}\, L_{\gamma,\mathrm{mod},0} n$, and $\mathrm{Q}\, L_{\gamma,\mathrm{mod},2} n$. To be able to compare the results, we consider the same setting with two offsets $\alpha = 1$ and $\alpha = 10$. Further, we choose $t_{\min} = 2\alpha + 0.1$, $t_{\max} = t_{\min} + 17$, $s_{\max} = 10$, and $N_s = N_t = 600$. Thus, the data are integral values of n over 216,000,000 ellipsoids. From this data the reconstruction is evaluated in the cross section $[-2.5, 5] \times \{0\} \times [1.5, 7]$ at uniformly distributed points where $N_{x_1} = 135$ and $N_{x_3} = 99$ values are used for the first and third coordinates, respectively. Finally, we use the trapezoidal rule to numerically compute the integrals with respect to θ in (4.4) and (4.5) and also in the reconstruction kernels (section 4.3). The numbers of uniformly distributed integration nodes are 201 for (4.4), 16 for (4.5), and 50 for the kernels.

Figure 6 displays the reconstructions with respect to Λ from (3.10). We recover all predicted visible singularities, i.e., all singularities are imaged except for the ones at the outermost points of the balls. Nevertheless, in case of $\alpha = 1$ singularities closer to the surface are more emphasized than the ones further away. For $\alpha = 10$ we make a different observation: the reconstructed intensity/contrast[2] of the singularities is nearly independent of the distance to the surface.

We defined the first modified reconstruction operator $\Lambda_{\mathrm{mod},0}$ in (3.9) to compensate the behavior of the top order symbol of Λ for small values of α compared to x_3. The results are in Figure 7. In comparison to the reconstructions in Figure 6 the intensity of the singularities for $\alpha = 1$ is significantly more uniform and more independent of their x_3-coordinate. However, in case of $\alpha = 10$ the contrast of the reconstructed singularities is less uniform than with Λ. It now increases with depth. These observations are in complete agreement with our theoretical considerations leading to the definition of $\Lambda_{\mathrm{mod},0}$ (see section 3.4).

[2]By the intensity or contrast of the reconstruction of a singularity $(x, \xi) \in \mathrm{WF}(n)$ we understand the number $\max\{|\,\mathrm{Q}\, \widetilde{L}_\gamma n(x) - \mathrm{Q}\, \widetilde{L}_\gamma n(p)| : p \text{ is a pixel in } B_\gamma(x)\}$ where $\widetilde{L}_\gamma$ denotes the imaging operator which is actually used. For an adequate choice of γ see Remark 5.2.

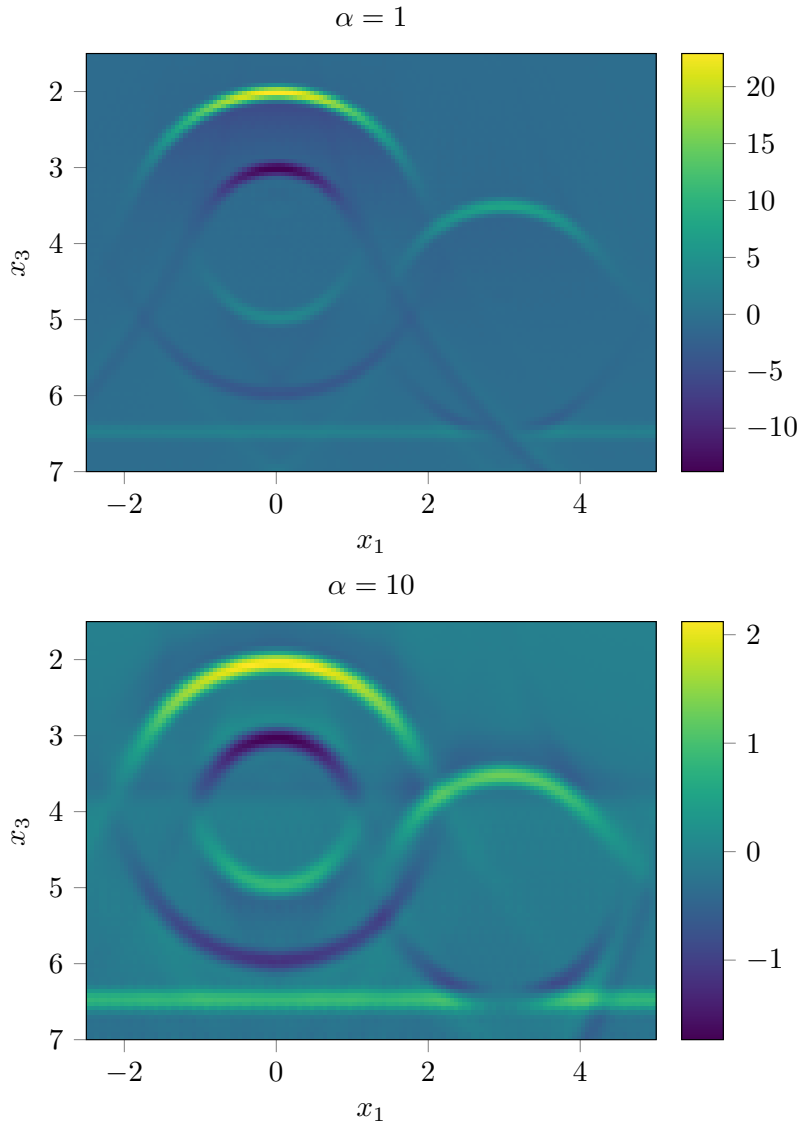

Figure 6. *Cross sections* $\mathrm{Q}\,L_\gamma n(\cdot, 0, \cdot)$ *for* Λ *from* (3.1). *They differ in the offset* α *and the regularization parameter* γ, *which depends on the offset. In case of* $\alpha = 1$ *we have* $\gamma = 0.2$, *for* $\alpha = 10$ *it is* $\gamma = 0.3$.

To achieve further improvements in case α is large compared to x_3, we introduced the operators $\Lambda_{\mathrm{mod},1}$ and $\Lambda_{\mathrm{mod},2}$; see (3.10). The approximation $\mathrm{Q}\,L_{\gamma,\mathrm{mod},1}n$ differs only slightly from those obtained by using $\mathrm{Q}\,L_{\gamma,\mathrm{mod},0}n$, thus they are not included here; we refer to [10, Fig. 5.18]. Figure 8 displays cross sections of $\mathrm{Q}\,L_{\gamma,\mathrm{mod},2}n$. As expected, adding the operator $\alpha^2\Lambda$ to $\Lambda_{\mathrm{mod},0}$ guarantees that the reconstructed contrast of singularities is independent of their depth coordinates, especially for α^2/x_3 large (image on the bottom of Figure 8).

To give an impression on the three-dimensional nature of our setting, we added two further cross sections with x_2-coordinates different from 0. In Figure 9 we present $\mathrm{Q}\,L_{\gamma,\mathrm{mod},0}n_*$, where

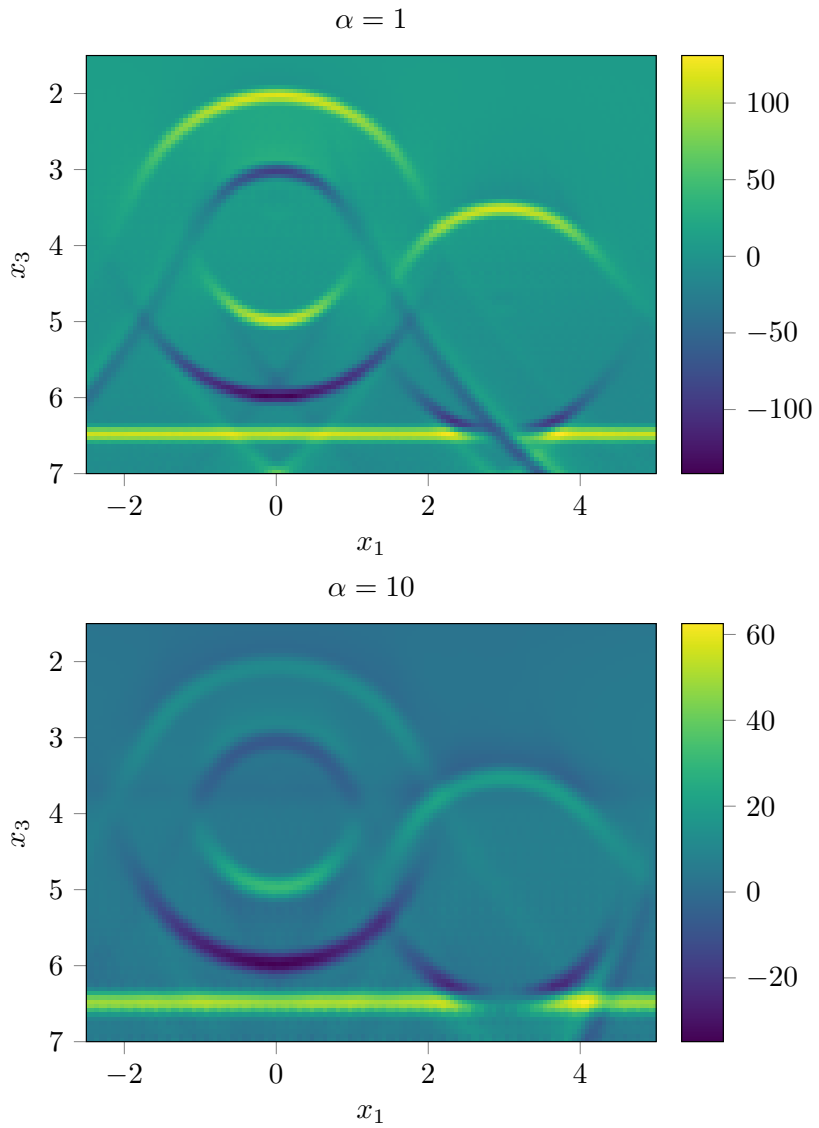

Figure 7. *Cross sections* $\mathrm{Q}\,L_{\gamma,\mathrm{mod},0}n(\cdot,0,\cdot)$ *for* $\Lambda_{\mathrm{mod},0}$ *from* (3.9). *Top:* $\alpha = 1$ *and* $\gamma = 0.2$*; bottom:* $\alpha = 10$ *and* $\gamma = 0.3$.

$n_* = n - \chi_{\{x_3 \geq 6.5\}}$, that is, n_* only consists of the characteristic functions of the balls. All parameters entering Q are chosen similarly as before.

Remark 5.1. In each of Figures 6–9, we see artifact curves that seem to come tangentially out of the location of the invisible singularities (red dots in Figure 5). A rough graph of the artifact curves shows that they seem to be along integration surfaces $E(s,t)$ for (s,t) in the boundary of the data set and for which the surface $E(s,t)$ is tangent to a boundary of the object. Limited data artifacts occur for the spherical transform along spheres tangent to object singularities and in the boundary of the data set [9] (see also [18]). Although those

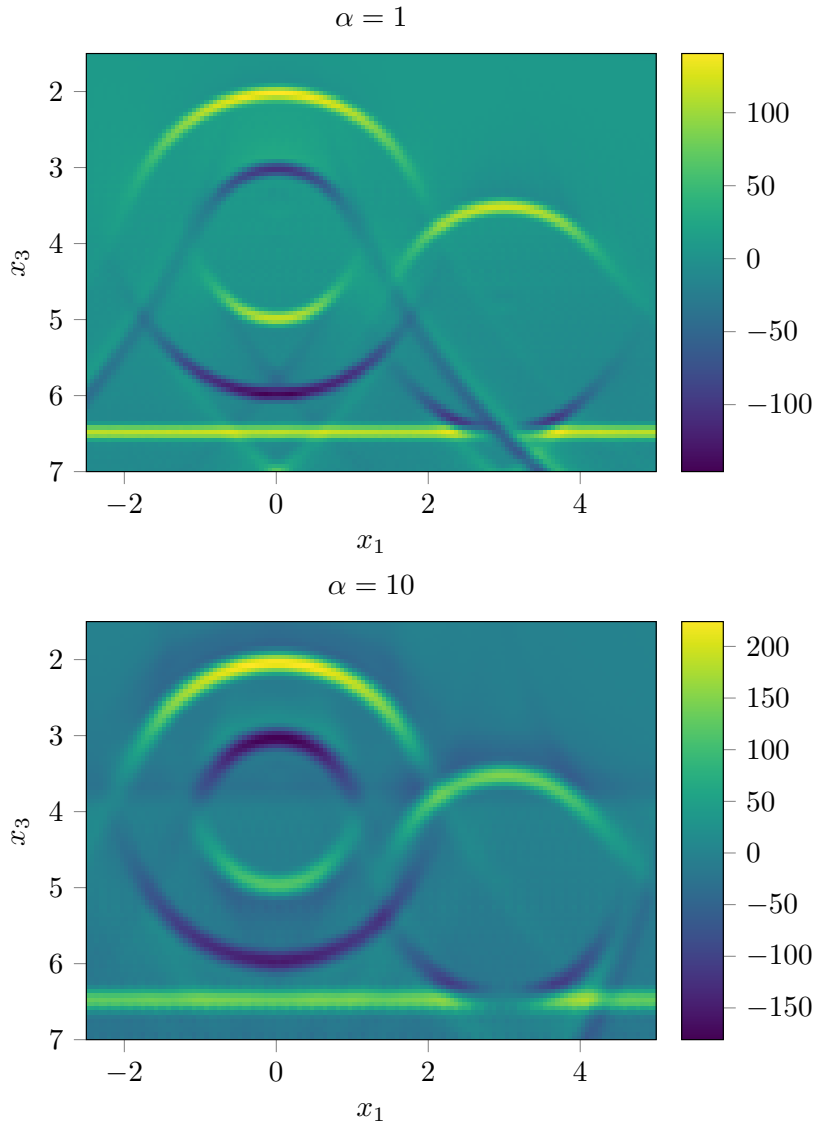

Figure 8. *Cross section* $\mathrm{Q}\, L_{\gamma,\mathrm{mod},2}(\cdot, 0, \cdot)$ *for* $\Lambda_{\mathrm{mod},2}$ *from* (3.10). *Top:* $\alpha = 1$ *and* $\gamma = 0.2$*; bottom:* $\alpha = 10$ *and* $\gamma = 0.3$.

results are for a different transform, they do suggest that some artifacts in Figures 6–9 are limited data artifacts.

One observes a second type of artifact, too, that is not tangent to a boundary of the object. If one compares the top image in Figures 6–8 with the top image of Figure 9 (that does not include a half space starting at $x_3 = 6.5$), one sees clearly that there are artifacts that seem to be independent of the disks and occur or are emphasized only when the half space is included. This was confirmed by reconstructions including just the half space and just the balls, and this could be the type of artifact coined "object-independent" in [5, Thm. 5.2]. In addition,

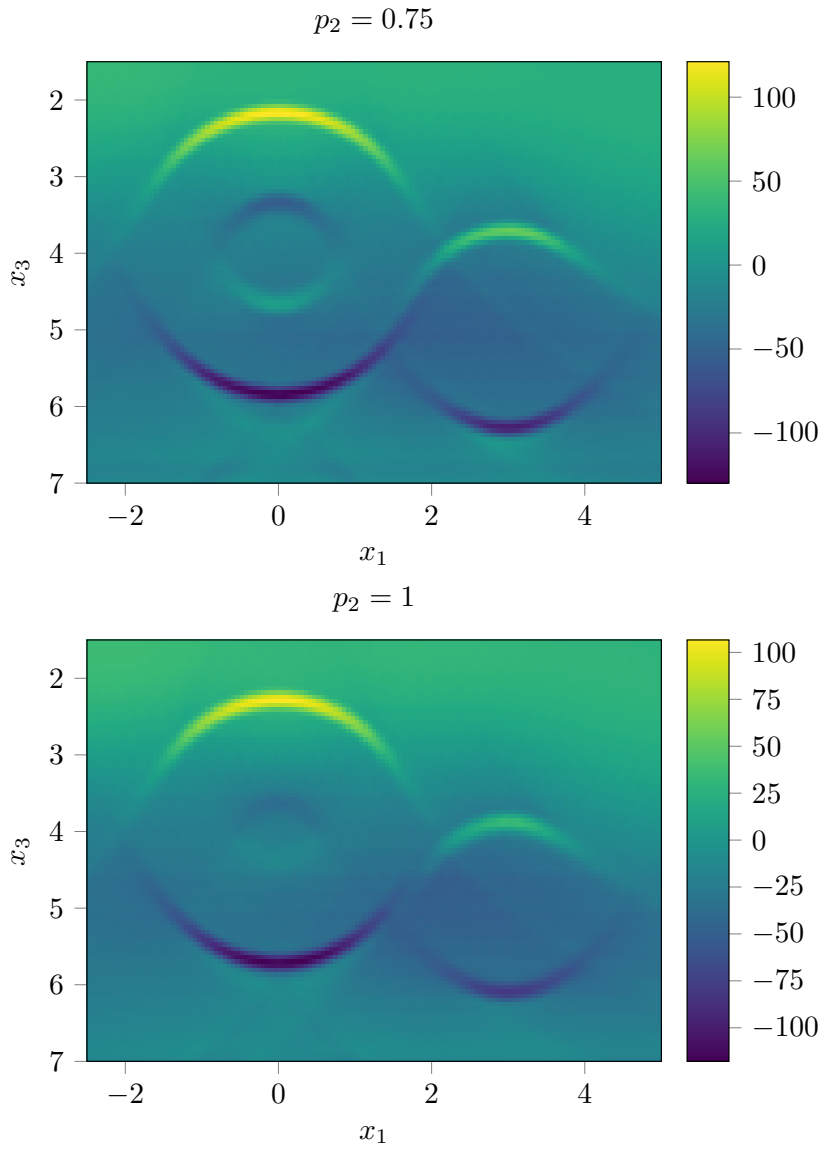

Figure 9. *Cross sections* $\mathrm{Q}\, L_{0.2,\mathrm{mod},0} n_*(\cdot, p_2, \cdot)$ *for* $\Lambda_{\mathrm{mod},2}$ *from* (3.10) *with* $\alpha = 1$. *Top:* $p_2 = 0.75$*; bottom:* $p_2 = 1$.

some streaks and other image degradation could occur for numerical reasons. Some of these numerical effects are described and named "endpoint artifacts" in [4, sect. 5.7]. However, they have not been analyzed rigorously, microlocally, and such analysis will appear in future work.

Finally, we point out that these artifacts can be suppressed by using a cutoff in s and t which gradually decreases to zero. This is described for the spherical transform in [9] and similar comments apply here.

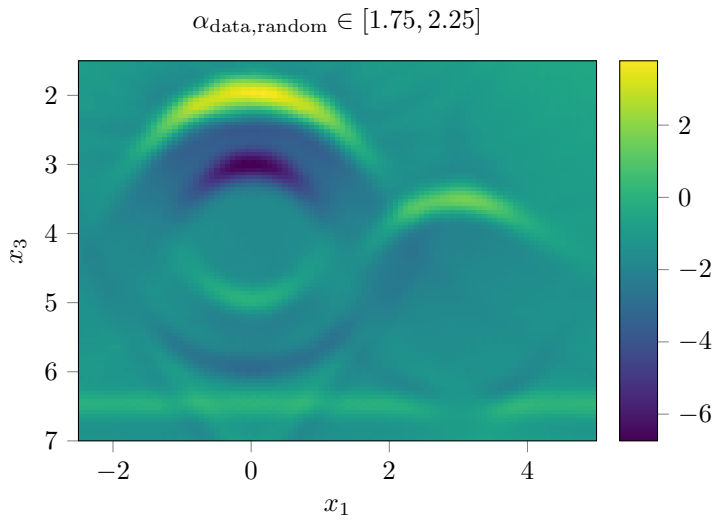

Figure 10. *Cross section* $\mathrm{Q}\, L_{0.4} n(\cdot, 0, \cdot)$ *with* Λ *from* (3.1). *The offset of the data differs randomly in* $[1.75, 2.25]$ *for each source/receiver pair, whereas the offset in* Q *is identically* 2.

In the next experiment we simulate a situation which very likely occurs in field measurements: the offset is not known exactly and differs slightly from one source/receiver pair to the next. In generating the data we therefore draw a different α for each source/receiver pair randomly and uniformly distributed from $[1.75, 2.25]$. The reconstruction, however, is done with the mean offset 2, that is, we set $\alpha = 2$ in the reconstruction kernel used in Q (for the values of the other parameters of Q see [10, sect. 5.3.2]). The result in Figure 10 is a bit blurry but the singular support is still clearly recognizable.

Remark 5.2. So far we have not commented on how we selected the scaling/regularization parameter γ, which depends on the discretization step sizes in Q, number of measurements, noise level, and offset. Finding a useful γ is a delicate task indeed. Our explanations and ideas from [11, Rem. 4.1] apply correspondingly.

5.2. Reconstructions using data from the wave equation. In the previous experiments we generated data with the same numerical scheme used to evaluate the reconstruction kernels. Here we provide data by solving the acoustic wave equation numerically. Thus, we avoid committing an inverse crime and additionally incorporate the modeling/linearization error; see section 2.

For generating the data y as in (2.5) we solve the acoustic wave equations (2.1) and (2.3) by the `PySIT` software [13] in the cuboid $[0.1, 0.8] \times [0.1, 1.0] \times [0.1, 0.8]$ with absorbing boundary conditions using perfectly matched layers. The discretization step size is 0.01 and on top of the cuboid 13×35 source and receiver pairs are positioned at $\mathbf{x}_{\mathrm{s}}(s) = (s_1, s_2 - \alpha, 0.1)^\top$ and $\mathbf{x}_{\mathrm{r}}(s) = (s_1, s_2 + \alpha, 0.1)^\top$ with $s_1 \in \{0.15 + 0.05i \,|\, i \in \{0, \dots, 12\}\}$, $s_2 \in \{0.125 + 0.025j \,|\, j \in \{0, \dots, 35\}\}$, and $\alpha = 0.025$. For the travel time t we take 1709 points between $t_{\min} = 0.1$ and $t_{\max} = 2$ into account. Further, the speed of sound ν in this experiment is

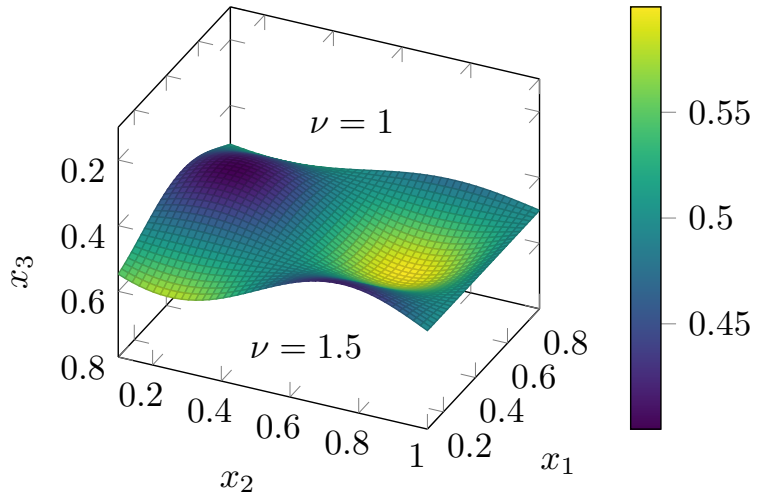

Figure 11. *An illustration of the speed of sound ν.*

$$\nu(x) = \begin{cases} 1 & \text{if } x_3 \leq 0.1\sin(2\pi x_2)\cos(2\pi x_1) + 0.5, \\ 1.5 & \text{if } x_3 > 0.1\sin(2\pi x_2)\cos(2\pi x_1) + 0.5, \end{cases}$$

which simulates two different materials; see Figure 11. The temporal impulse at time $t = 0$, that is, the source is modeled by a scaled and truncated Gaussian.

Figure 12 shows on the left four cross sections of the interface we want to reconstruct. All singularities that appear have a nonvanishing third component in their normal directions, so we expect to see them all in the corresponding reconstructions on the right, which are obtained from (5.2) using the kernel of $\Lambda_{0.07}$ with Λ from (3.1) (the used cutoff function is an adapted version of (5.1)).

In all reconstructed cross sections, the singular support, which is the boundary between the two different material layers, is reconstructed as a relatively thick curve. This is due to a lack of data, more precisely, due to a large sampling rate for Fn which restricts from below the smallest detail which is represented in the data; see, e.g., [17, Chap. III].

Further, the reconstructed singularities near to the left boundary of the cuboid are less visible than the ones near to the right. The reason is that on the left the first receiver is farther away from the boundary.

If we compare the two cross sections $x_1 = 0.1$ and $x_1 = 0.5$, we notice that all reconstructed singularities in case of $x_1 = 0.5$ have nearly the same intensity, whereas for $x_1 = 0.1$ there are big differences. This effect is due to location of the cross sections inside the cuboid. There are more sources and receivers in the middle of the cuboid than at the boundary as there are no pairs of sources and receivers in front of it, i.e., for $x_1 < 0.1$.

At last, we remark that in all four cross sections the contrast of the singularities at the boundaries depends on how the interface hits the boundary. By Theorem 3.8 and the consequences of Proposition 3.10 (see (5.3) and (5.4), for instance), the imaging operator

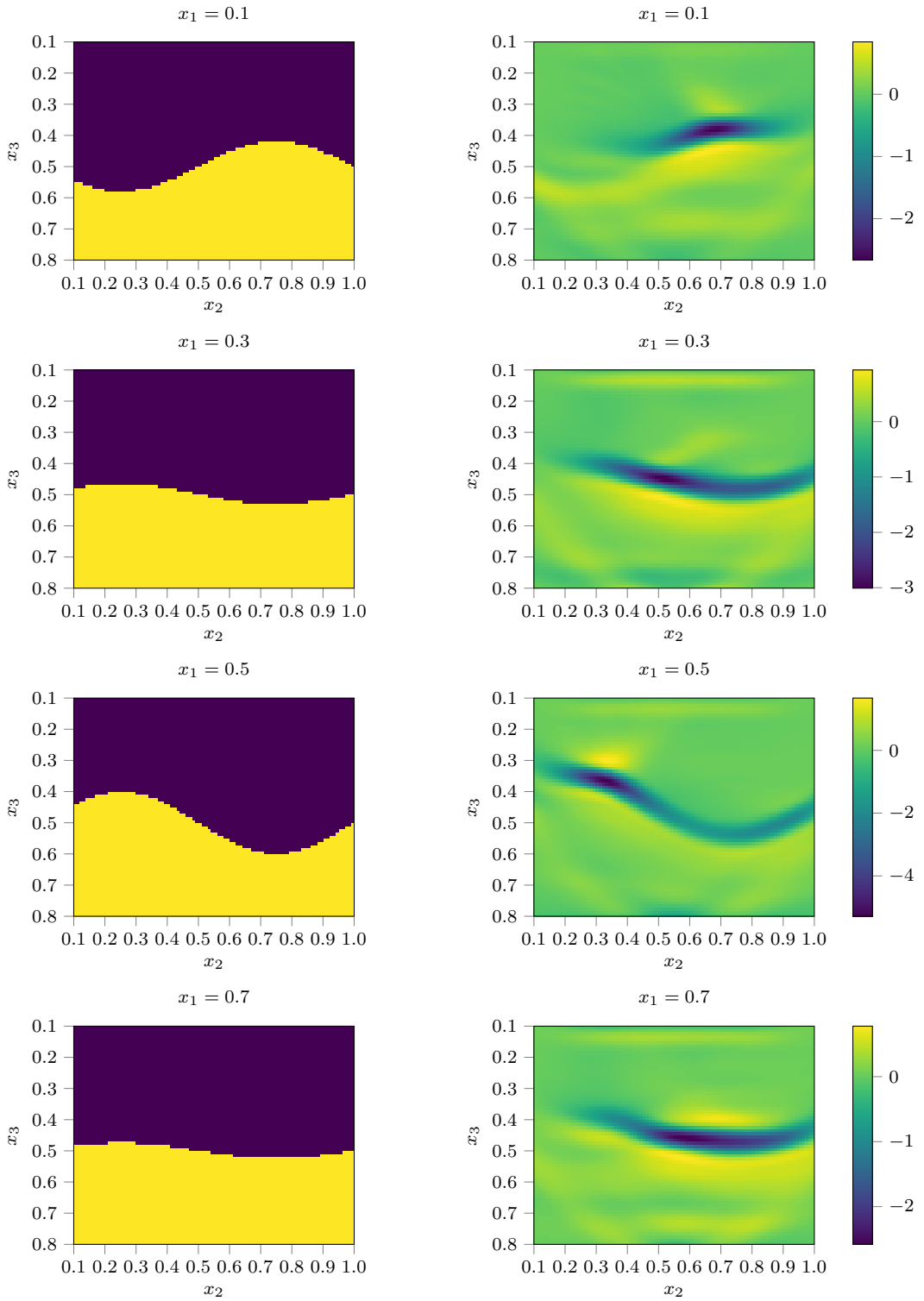

Figure 12. *Ground truth (left) and the corresponding reconstructions* $\mathrm{Q}\, L_{0.07} n$ *with* Λ *from* (3.1).

preserves a singularity of n only if there is an ellipse being integrated over which is tangent to that singularity.

Remark 5.3. In [11, sect. 4.2] we included a numerical experiment, in two dimensions though, which takes a further modeling error into account: the required reference solution of the wave equation is not computed with the constant sound speed 1 but with a spatially varying sound speed. This works remarkably well.

Acknowledgments. The authors thank the referees for insightful comments that improved the article. Todd Quinto thanks his undergraduate NSF REU research students Elise Cho and Brian Parkes for their work on artifacts that strengthened Remark 5.1.

REFERENCES

[1] L.-E. Andersson, *On the determination of a function from spherical averages*, SIAM J. Math. Anal., 19 (1988), pp. 214–232, https://doi.org/10.1137/0519016.

[2] G. Beylkin, *The inversion problem and applications of the generalized Radon transform*, Comm. Pure Appl. Math., 37 (1984), pp. 579–599, https://doi.org/10.1002/cpa.3160370503.

[3] G. Beylkin, *Imaging of discontinuities in the inverse scattering problem by inversion of a causal generalized Radon transform*, J. Math. Phys., 26 (1985), pp. 99–108, https://doi.org/10.1063/1.526755.

[4] N. Bleistein, J. K. Cohen, and J. W. Stockwell, Jr., *Mathematics of Multidimensional Seismic Imaging, Migration, and Inversion*, Interdiscip. Appl. Math. 13, Springer-Verlag, New York, 2001, http://dx.doi.org/10.1007/978-1-4613-0001-4.

[5] L. Borg, J. Frikel, J. S. Jørgensen, and E. T. Quinto, *Analyzing reconstruction artifacts from arbitrary incomplete X-ray CT data*, SIAM J. Imaging Sci., 11 (2018), pp. 2786–2814, https://doi.org/10.1137/18M1166833.

[6] J. K. Cohen and N. Bleistein, *Velocity inversion procedure for acoustic waves*, Geophysics, 44 (1979), pp. 1077–1085, http://dx.doi.org/10.1190/1.1440996.

[7] M. V. de Hoop, H. Smith, G. Uhlmann, and R. D. van der Hilst, *Seismic imaging with the generalized Radon transform: A curvelet transform perspective*, Inverse Problems, 25 (2009), 025005, http://dx.doi.org/10.1088/0266-5611/25/2/025005.

[8] R. Felea, V. P. Krishnan, C. J. Nolan, and E. T. Quinto, *Common midpoint versus common offset acquisition geometry in seismic imaging*, Inverse Probl. Imaging, 10 (2016), pp. 87–102, https://doi.org/10.3934/ipi.2016.10.87.

[9] J. Frikel and E. T. Quinto, *Artifacts in incomplete data tomography with applications to photoacoustic tomography and sonar*, SIAM J. Appl. Math., 75 (2015), pp. 703–725, https://doi.org/10.1137/140977709.

[10] C. Grathwohl, *Seismic Imaging with the Elliptic Radon Transform in 3D: Analytical and Numerical Aspects*, Ph.D. thesis, Karlsruhe Institute of Technology, 2020, https://doi.org/10.5445/IR/1000105093.

[11] C. Grathwohl, P. Kunstmann, E. T. Quinto, and A. Rieder, *Approximate inverse for the common offset acquisition geometry in 2D seismic imaging*, Inverse Problems, 34 (2018), 014002, https://doi.org/10.1088/1361-6420/aa9900.

[12] C. Grathwohl, P. Kunstmann, E. T. Quinto, and A. Rieder, *Microlocal analysis of imaging operators for effective common offset seismic reconstruction*, Inverse Problems, 34 (2018), 114001, https://doi.org/10.1088/1361-6420/aadc2a.

[13] R. J. Hewett and L. Demanet, *PySIT: Python Seismic Imaging Toolbox*, 2020, https://doi.org/10.5281/zenodo.3603367.

[14] L. Hörmander, *Fourier Integral Operators*, I, Acta Math., 127 (1971), pp. 79–183.

[15] V. P. Krishnan, H. Levinson, and E. T. Quinto, *Microlocal Analysis of Elliptical Radon Transforms with Foci on a Line*, in The Mathematical Legacy of Leon Ehrenpreis, 1930-2010, I. Sabadini and D. Struppa, eds., Springer Proc. Math. 16, Springer, New York, 2012, pp. 163–182, http://dx.doi.org/10.1007/978-88-470-1947-8_11.

[16] A. K. Louis, *Approximate inverse for linear and some nonlinear problems*, Inverse Problems, 11 (1995), pp. 1211–1223, http://stacks.iop.org/0266-5611/11/1211.
[17] F. Natterer, *The Mathematics of Computerized Tomography*, Classics in Appl. Math. 32, SIAM, Philadelphia, 2001, http://dx.doi.org/10.1137/1.9780898719284.
[18] L. V. Nguyen, *On artifacts in limited data spherical Radon transform: Flat observation surfaces*, SIAM J. Math. Anal., 47 (2015), pp. 2984–3004, https://doi.org/10.1137/140980740.
[19] C. J. Nolan and W. W. Symes, *Global solution of a linearized inverse problem for the wave equation*, Comm. Partial Differential Equations, 22 (1997), pp. 919–952, https://doi.org/10.1080/03605309708821289.
[20] B. Petersen, *Introduction to the Fourier Transform and Pseudo-Differential Operators*, Pitman, Boston, 1983.
[21] E. T. Quinto, *The dependence of the generalized Radon transform on defining measures*, Trans. Amer. Math. Soc., 257 (1980), pp. 331–346, https://doi.org/10.2307/1998299.
[22] E. T. Quinto, A. Rieder, and T. Schuster, *Local inversion of the sonar transform regularized by the approximate inverse*, Inverse Problems, 27 (2011), 035006, https://doi.org/10.1088/0266-5611/27/3/035006.
[23] Rakesh, *A linearised inverse problem for the wave equation*, Comm. Partial Differential Equations, 13 (1988), pp. 573–601, https://doi.org/10.1080/03605308808820553.
[24] M. A. Shubin, *Pseudodifferential Operators and Spectral Theory*, Springer Ser. Sov. Math., Springer-Verlag, Berlin, 1987.
[25] C. C. Stolk, *Microlocal analysis of a seismic linearized inverse problem*, Wave Motion, 32 (2000), pp. 267–290, https://doi.org/10.1016/S0165-2125(00)00043-3.
[26] W. W. Symes, *Mathematics of Reflection Seismology*, Tech. report, The Rice Inversion Project, Rice University, Houston, TX, 1998, http://www.trip.caam.rice.edu/downloads/preamble.pdf.